

# Comprehensive broad-band study of accreting neutron stars with *Suzaku*: Is there a bi-modality in the X-ray spectrum?

Pragati Pradhan<sup>1,2\*</sup>, Biswajit Paul,<sup>3</sup> Enrico Bozzo<sup>4</sup>, Chandreyee Maitra<sup>5</sup> and B. C. Paul<sup>6</sup>

<sup>1</sup>Massachusetts Institute of Technology, Kavli Institute for Astrophysics and Space Research, Cambridge, MA 02139, USA

<sup>2</sup>St. Joseph's College, Singamari, Darjeeling 734104, West Bengal, India

<sup>3</sup>Raman Research Institute, Sadashivnagar, Bangalore 560080, India

<sup>4</sup>ISDC, University of Geneva, Chemin d'Ecogia 16, CH-1290 Versoix, Switzerland

<sup>5</sup>Max Planck Institute for Extraterrestrial Physics, D-85748 Garching, Germany

<sup>6</sup>North Bengal University, Department of Physics, Raja Rammohanpur, District Darjeeling 734013, West Bengal, India

Accepted 2020 December 24. Received 2020 December 5; in original form 2020 February 22

## ABSTRACT

We present a broad-band spectral analysis of accreting neutron stars using data from XIS and PIN onboard *Suzaku*. From spectral fits of these sources with a single continuum model including a power law and high energy cut-off, cyclotron lines (where required), we studied the correlation between various spectral parameters. Among 39 sources we studied, 16 are those where the existence of a cyclotron line is known in literature, and 29 need a cut-off energy. Among these 29 sources, 18 have cut-off energy bunched in a range of 3–10 keV while for 11 sources, it spreads over 12–25 keV. This bi-modal behaviour is not based on the specific nature of the systems being a Be XRB or supergiant HMXB, nor on different beaming patterns characterizing their X-ray emission (as inferred from simultaneous study of their pulse profiles). The broad-band coverage of *Suzaku* also shows that the cut-off energies saturate for higher values of cyclotron line energies – consistent with previous works in literature – for both the groups and the width of the cyclotron line show a weak correlation with the cyclotron line energy. We also find an anticorrelation with luminosity for both spectral index and folding energy, respectively. Unlike previous works, we did not detect any anticorrelation between X-ray luminosity and EW of K $\alpha$  lines. Finally, we show that the EW and flux of the iron K $\alpha$  line are smaller in SFXTs than classical NS-HMXBs. We discuss these findings in terms of different properties of stellar winds and accretion mechanisms.

**Key words:** accretion, accretion discs – pulsars: general – X-rays: binaries.

## 1 INTRODUCTION

High-mass X-ray binaries (HMXBs) are binary systems comprising a compact object and a massive star orbiting around a common centre of mass. The compact object can be either a neutron star or a black hole. In this work, we mainly deal with HMXBs that harbour a neutron star as the compact object accreting from the powerful wind of the massive companion (White, Swank & Holt 1983; Nagase 1989; Bildsten et al. 1997). These neutron stars in HMXBs have magnetic fields of the order of  $\gtrsim 10^{12}$  G. The accreted material is thus expected to be channelled along the magnetic field lines at relatively large distances from the compact object, leading to the formation of extended accretion columns. The exact details of how the magnetic field affects the accretion flow is still a topic of investigation (Becker & Wolff 2007). It is generally expected that the inflowing material is directed towards the magnetic poles of the neutron star where two hot spots are formed. The gravitational potential energy of the inflowing material is first converted into kinetic energy and then released as X-rays due to shocks and dissipations into the accretion column and on the hot spots (Basko & Sunyaev 1975). If the rotation axis and the magnetic axis of the neutron star are not completely aligned, the X-

ray emission from the source appears pulsed to any distant observer whose line of sight to the object intersects the beam periodically.

The high magnetic fields of neutron stars can be measured from the cyclotron resonance scattering features (CRSFs). These features are known to be produced as a consequence of cyclotron resonant scattering of X-ray photons in the presence of an intense magnetic field. Their centroid energy is related to the NS magnetic field intensity by the equation:

$$E_C = 11.6 \frac{B}{10^{12} \text{ G}} (1+z)^{-1} \text{ keV}, \quad (1)$$

where  $z$  is the gravitational redshift.

Classical HMXBs can be classified as either Be/X-ray binaries (BeXBs; Reig 2011) or Supergiant X-ray binaries (SGXBs; Walter et al. 2015). Relatively recently discovered HMXBs with supergiant companions, called Supergiant Fast X-ray Transients (SFXTs), are characterized by short outbursts with fast rise times ( $\sim$  tens of minutes) and typical durations of a few hours (Sguera et al. 2006). For this study, along with both classical HMXBs and SFXTs observed with *Suzaku* (Mitsuda et al. 2007), we have also included a few sources which have a low mass companion star but are known to harbour neutron star with strong magnetic fields. These four sources are Her X-1, 4U 1626-67, GX 1+4, and 4U 1822-37 and have been classified here as low mass X-ray binaries, LMXBs (although strictly speaking, Her X-1 is an intermediate mass X-ray binary).

\* E-mail: [pragati2707@gmail.com](mailto:pragati2707@gmail.com)

## 2 DATA REDUCTION

*Suzaku* (Mitsuda et al. 2007) is a broad-band X-ray observatory covering the energy range 0.2–600 keV. There are two main instruments on-board *Suzaku*: the X-ray Imaging Spectrometer XIS (Koyama et al. 2007), covering the 0.2–12 keV energy range, and the hard X-ray detector (HXD). The XIS consists of four CCD detectors of which three (XIS 0, 2, and 3) are front illuminated (FI) and one (XIS 1) is back illuminated (BI). The HXD comprises PIN diodes (Takahashi et al. 2007) that cover the 10–70 keV energy range and GSO crystal scintillator detectors that cover the 70–600 keV energy range.

For the XIS and the HXD data, we used the filtered cleaned event files which are obtained using the pre-determined screening criteria as suggested in the *Suzaku* ABC guide.<sup>1</sup> The data reduction for both instruments was carried out following the reduction technique mentioned in the same *Suzaku* ABC guide. We applied the barycentric correction to all event files using `aepipeline`. For the XIS data reduction we applied the following procedure: for sources that showed jitters in the image, the event files were corrected by using the `aeattcorr` and `xiscoord` tools to update the attitude information; for those sources affected by pile-up, we discarded photons collected within the portion of the PSF where the estimated pile-up fraction was greater than 4 per cent. This was done by using the FTOOLS task `pileest`. XIS spectra were then extracted by choosing circular regions of 2, 3, or 4 arcmin radius from the source position depending on whether the observation was made in 1/8, 1/4, or 0 window mode, respectively. Background spectra for the XIS were extracted by selecting regions of the same size as mentioned above in a portion of the CCD that was not significantly contaminated by the source X-ray emission. For relatively fainter objects observed in window ‘Off’ mode (like IGR J16493-4348, IGR J16465-4507, IGR J16479-4514, and IGR J08408-4503) choosing the same radius for the source and background extraction region gave rise to a dip-like artefact in the spectra visible around 6 keV. Hence, for these sources, a larger background region was chosen by adopting an annulus with inner (outer) radius of 5 arcmin (7 arcmin) centred on the source best known position.

The PIN source spectra were additionally corrected for dead-time effects by using the FTOOLS task `hxddtcor`. For the HXD/PIN, simulated ‘tuned’ non X-ray background event files (NXB) corresponding to the month and year of the respective observations were used to estimate the non X-ray background<sup>2</sup> (Fukazawa et al. 2009).

The XIS spectra were extracted with 2048 channels and the PIN spectra with 255 channels. Response files for the XIS were created using the CALDB version ‘20150312’. For the HXD/PIN spectrum, response files corresponding to the epoch of the observation were obtained from the *Suzaku* guest observer facility.<sup>3</sup>

The sources considered for this study and all the OBSID corresponding to the observations used are listed in Table 1.

## 3 SPECTRAL ANALYSIS

For the spectral analysis of the selected sources, we have used the spectra from all the available XIS units (0, 1, 2, and 3) and the PIN. In some cases we noticed systematic differences between the spectra obtained from the BI XIS 1 and the rest of the XIS units. In all these cases, we did not make use of the BI XIS 1 data in the spectral

fitting as they gave no additional information and led to a poorer fit with larger  $\chi^2_{\text{red}}$ . Spectral fitting was performed by using XSPEC v12.9.0. Artificial residuals are known to arise in the XIS spectra around the Si edge and the Au edge. We have thus discarded the energy range  $\sim 1.7$ –2.3 keV for spectral analysis. For most sources, we have limited our analysis to the energy range  $\sim 0.8$ –10.0 keV for XIS and 15.0–70.0 keV for the HXD-PIN. For sources like OAO 1657-415, 4U 1909+07, IGR J16393-4643, GX 301-2, and GX 1+4 where the absorption at soft X-ray is larger, we did not use data below  $\sim 3$  keV either due to the poor signal-to-noise ratio (S/N) or because the spectra below 3 keV show a ‘low energy tail’ which is not characteristic of the source but has an instrumental origin (Suchy et al. 2012). For other sources characterized by a PIN spectrum with limited statistics, like V 0332+53, 4U 1909+07, IGR J16393-4643, 4U 2206+54, SW J2000.6+3210, and 4U 1822-37, we have discarded the data points in the PIN spectrum, above the energy where the S/N is very low. For some sources like 4U 1907+09, 4U 1700-37, and IGR J17544-2619, we noticed an excess above the power-law continuum in the data around 10 keV, with an amplitude of 10 per cent, 10 per cent and 5 per cent, respectively. This ‘10 keV’ feature was also previously reported in the cases of 4U 1907+09 and 4U 1538-522 (Coburn et al. 2002; Rivers et al. 2010). Since the aim of this work is to perform a homogeneous fit as much as possible, we discarded in all cases the data around this feature.

For IGR J16318-4848, we limited our analysis to the energy range 5.0–60.0 keV, owing to very strong absorption below 5.0 keV and the low S/N above 60 keV (Barragán et al. 2009). For seven sources (IGR J16195-4945, IGR J16493-4348, IGR J16465-4507, IGR J16479-4514, IGR J17391-3021, IGR J08408-4503, and IGR J00370+6122), we could make use only of the XIS data as their PIN spectrum was contaminated either by nearby bright sources, or by the diffuse emission from Galactic Ridge, or due to the high CXB and NXB (Sidoli, Esposito & Ducci 2010; Bodaghee et al. 2011; Sidoli et al. 2013). For eclipsing HMXBs like Her X-1, LMC X-4, Cen X-3, 4U 1700-37, 4U 1538-522, SMC X-1, Vela X-1, OAO 1657-415, 4U 1822-37, IGR J16479-4514, and IGR J16195-4945, we have checked whether the source was in eclipse or not during the considered observations by folding its light curve together with the corresponding RXTE-ASM orbital light curve<sup>4</sup> at the known orbital period of the source. Except for Cen X-3, IGR J16479-4514, and 4U 1822-37, all the other sources were not observed during an X-ray eclipse. For Cen X-3 and IGR J16479-4514, we have extracted the time filtered spectrum corresponding to the times when the source was not in eclipse. For Cen X-3 we extracted spectra only for ‘Segment E’ of Naik, Paul & Ali (2011) while for IGR J16479-4514, we extracted the spectrum starting 143 ks after the beginning of the observation (as is done in Sidoli et al. 2013). For 4U 1822-37, the full *Suzaku* observation spanned nearly four times the orbital period of the neutron star. Hence for 4U 1822-37, we extracted a spectrum only for that phase interval during which the source was outside the dips and eclipse (0.1–0.6 when Phase 0 is at MJD 54010.48). In the cases of Vela X-1 and 4U 1538-522, spectra were extracted only for that part of the observation during which the hardness ratio remained relatively stable as done in Maitra & Paul (2013b) and Hemphill et al. (2014).

We fitted the spectra of all sources by using all available instruments simultaneously. We kept all spectral parameters of the different instruments tied together during the fit. Only the intercalibration constants were left free to vary. We have used the most commonly

<sup>1</sup><http://heasarc.gsfc.nasa.gov/docs/suzaku/analysis/abc/>

<sup>2</sup><https://heasarc.gsfc.nasa.gov/docs/suzaku/analysis/pinbgd.html>

<sup>3</sup><https://heasarc.gsfc.nasa.gov/docs/heasarc/caldb/suzaku/>

<sup>4</sup><https://heasarc.gsfc.nasa.gov/docs/xte/ASM/sources.html>

**Table 1.** Observation log and distances to the different sources considered in this paper.

Source	OBSID	Window mode	Distance (kpc)	Reference
Her X-1	100035010	1/8	6.6 ± 0.4	Reynolds et al. (1997)
4U 0115+63	406049010	1/4	7.0 ± 0.3	Riquelme, Torrejón & Negueruela (2012)
Cen X-3	403046010	1/4	5.7 ± 1.5	Thompson & Rothschild (2009)
4U 1626-67	400015010	1/8	5-13	Chakrabarty (1998)
XTEJ1946+274	405041010	1/4	9.5 ± 2.9	Wilson et al. (2003)
Vela X-1	403045010	1/4	1.9 ± 0.2	Sadakane et al. (1985)
4U 1907+09	401057010	1/4	2.8 <sup>+5.0</sup> <sub>-1.8</sub>	Nespoli, Fabregat & Mennickent (2008)
4U 1538-522	407068010	1/4	6.4 ± 1	Reynolds, Bell & Hilditch (1992)
GX 301-2	403044010	1/4	3.04*	Kaper, van der Meer & Najarro (2006)
1 A1118-61	403049010	1/4	5.2 ± 0.9	Riquelme et al. (2012)
4U 0114+65	406017010	1/4	7.0 ± 3.6	Reig et al. (1996)
GX 304-1	905002010	1/4	2.4 ± 0.5	Parkes, Murdin & Mason (1980)
OA0 1657-415	406011010	1/4	6.4 ± 1.5	Chakrabarty et al. (2002)
Cep X-4	409037010	1/4	3.8 ± 0.6	Bonnet-Bidaud & Mouchet (1998)
4U 1700-37	401058010	1/4	2.12 ± 0.34	Megier et al. (2009)
A 0535+026	404054010	1/4	2.00 ± 0.7	Steele et al. (1998)
4U 1822-37	401051010	1/4	2.5 <sup>+3.0</sup> <sub>-1.9</sub>	Mason & Cordova (1982)
GX 1+4	405077010	1/4	3-15	Chakrabarty & Roche (1997)
GRO J1008-57	902003010	1/4	5*	Coe et al. (1994)
4U1909+07	405073010	1/4	7.00 ± 3.0	Morel & Grosdidier (2005)
IGR J16393-4643	404056010	Off	10.6*	Chaty et al. (2008)
4U 2206+54	402069010	1/4	2.90 ± 0.20	Riquelme et al. (2012)
SW J2000.6+3210	401053020	Off	8*	Masetti et al. (2008)
LMC X-4	702036020	1/8	50*	Hung et al. (2010)
KS1947+300	908001020	1/4	10.4 ± 0.9	Riquelme et al. (2012)
EXO 2030+375	402068010	1/4	7.1 ± 0.2	Wilson et al. (2002)
SMC X-1	706030100	Off	60.0*	Neilsen, Hickox & Vrtiliek (2004)
V 0332+53	904004010	1/4	7.5 ± 1.50	Negueruela et al. (1999)
IGR J16493-4348	401054010	Off	2-3	Hill et al. (2008)
IGRJ16318-4848	401094010	Off	3.60 ± 2.60	Filliatre & Chaty (2004)
IGRJ16207-5129	402065020	1/4	6.10 <sup>+8.90</sup> <sub>-3.50</sub>	Nespoli et al. (2008)
IGR J18410-0535	505090010	Off	3.2 <sup>+2.0</sup> <sub>-1.5</sub>	Nespoli et al. (2008)
IGR J17544-2619	402061010	1/4	3.20 ± 1.00	Pellizza, Chaty & Negueruela (2006)
IGR J16195-4945	401056010	Off	5*	Tomsick et al. (2006)
IGR J16465-4507	401052010	Off	9.5 <sup>+14.1</sup> <sub>-5.7</sub>	Heras & Walter (2004)
IGR J16479-4514	406078010	Off	7.50 ± 2.50	Chaty et al. (2008)
IGR J17391-3021	402066010	1/4	2.7*	Rahoui et al. (2008)
IGR J08408-4503	404070010	Off	3.0*	Masetti et al. (2006)
IGR J00370+6122	402064010	1/4	3.3*	Reig et al. (2005)

Note. \* Distance error is not known so error is assumed as 1 kpc.

adopted models to describe the high energy emission of HMXBs and LMXBs consisting of a power-law component with a high energy cut-off (HIGHECUT; White et al. 1983; Coburn et al. 2002). This model gave formally acceptable fits ( $\chi^2_{\text{red}} = 0.89-1.45$ ) to all data, the only exceptions being A0535+026, LMC X-4, and GX 1+4. In these three cases, the NPEX (Mihara 1995; Makishima et al. 1999), FDCUT (Tanaka 1986), and NEWHCUT (Burderi et al. 2000) models, respectively, provided a better description of the data. We noticed that no formal acceptable fit could be obtained with the selected models to the data of GX 1+4 ( $\chi^2_{\text{red}} = 1.66$ ) and thus we decided not to include this source for the discussion on the spectral parameters' correlations. Such a high value of  $\chi^2_{\text{red}}$  for GX 1+4 has also been reported in a recent analysis of the same data set to which refer the readers for further details (Yoshida et al. 2017).

Furthermore, although we fit Her X-1 and 4U 0115+63 with the HIGHECUT model, we did not include their CRSF parameters for correlation studies. The reason being that the former is known to show a complicated cyclotron energy variation (Staubert et al. 2014) and for latter, the CRSF lie at  $\sim 11$  keV, which is outside the usable PIN band (Kühnel et al. 2020).

The analytical form of the main model considered in this work: HIGHECUT is

$$\text{HIGHECUT}(E) = A E^{-\Gamma} \times \begin{cases} 1 & (E \leq E_{\text{cut}}) \\ e^{-(E-E_{\text{cut}})/E_{\text{fold}}} & (E > E_{\text{cut}}) \end{cases} \quad (2)$$

(where  $\Gamma$  is the photon index,  $E_{\text{cut}}$  the cut-off energy, and  $E_{\text{fold}}$  the folding energy),

For other sources where the cut-off energy was not required (IGR J16195-4945, IGR J16493-4348, IGR J16465-4507, IGR J16479-4514, IGR J17391-3021, IGR J08408-4503, and IGR J00370+6122), we fitted the spectrum with a simple power law corrected for photoelectric absorption. In many of the analysed sources, CRSFs were clearly detected as broad absorption features in the X-ray spectra. Where required, those features have been fit with pseudo Lorentzian optical depth profiles (CYCLABS in Xspec). We used additional Gaussian components to take into account the presence of emission lines, mostly due to the fluorescence of neutral iron. In addition to the above components, in some cases, a partial covering model and/or blackbody component was used to account for fractional local absorption and for thermal emission components

in the spectrum, respectively. The best-fitting continuum parameters for all the sources are reported in Table 2. The harmonics of the detected cyclotron line are given in Table 3. We report in Table 4 all significantly measured emission lines.

It should be noted here that to have an overview and for the purpose of this analysis, we have mostly considered X-ray spectrum over the entire observation as the representative of that source – except eclipses and a few observations showing large variation in spectrum which were filtered likewise as mentioned earlier. The details on the X-ray variability of the sources that we have considered can be found in the already published papers on the corresponding data (see e.g. Maitra & Paul 2013a,b; Pradhan et al. 2013, 2014, 2015). While such studies on short-term variability study will help addressing the effect of the wind inhomogeneities on the overall accretion process on time-scales as short as tens to hundreds of seconds, the average spectrum considered in this work allows a clean and relatively straightforward comparison between the different classes and sub-classes of sources independent from the short-term variation of the winds which are washed out on the long integration times we used in the analysis here.

We should also mention here that our choice of HIGHECUT model is motivated by finding a representative model to fit all our sources while at the same time having the least degeneracy between model parameters. Since HIGHECUT has shown to have the least degeneracy while describing the X-ray spectra of accreting neutron stars (Coburn et al. 2002), we use this model throughout our analysis. To minimize degeneracy in fitting though, we have cross-checked the fitting parameters at each step to literature values (where available), and if it is physical. We are therefore confident that the correlation presented in this paper is real within the limits to what a phenomenological model can provide.

## 4 RESULTS

The main purpose of this work is to carry out a correlation study among the various spectral parameters that are measured from known HMXBs and a few strong magnetic field LMXBs observed by *Suzaku*. We have also investigated the variation of the spectral parameters with luminosity,  $L_X$ . The distances used for  $L_X$  calculations<sup>5</sup> are reported in Table 1.  $L_X$  is calculated over the energy range for which the individual spectra were fitted. For most sources, it is 0.8–70.0 keV. In other cases, as mentioned in Section 3, we have discarded spectral data below 3 keV. Due to the relatively high absorption, we verified that in these cases the difference in the luminosity estimated in the 0.8–70 keV and 3.0–70.0 keV bands are negligible. We also verified that for those sources where the PIN spectrum is truncated prior to 70 keV due to the poor S/N (mentioned in Section 3), the X-ray luminosity evaluated in the energy range of the fit or in the full 0.8–70.0 keV energy range would not change significantly. All the fainter sources for which only the XIS spectrum is used, are marked in grey in all relevant figures. We discuss in the following sub-sections all the correlations between the different parameters that we could find from the analysis of the *Suzaku* data of the considered sources.

### 4.1 Correlation among the spectral parameters

#### 4.1.1 $E_{\text{cut}}$ versus $L_X$

When the measured values of the  $E_{\text{cut}}$  are plotted against  $L_X$ , we note a bimodality in the  $E_{\text{cut}}$  distribution (see Fig. 1). For clarity, we have

<sup>5</sup>For sources where distance errors are not determined, we assumed an error of 1 kpc.

used different colour schemes to distinguish the two groups. The upper branch where the cut-off energy range from  $\sim 12$ –25 keV (henceforth Branch 1) has been plotted in blue while the lower branch which have cut-off energy range of 3–10 keV (henceforth Branch 2) has been plotted in magenta. Although there is not a clear correlation or anticorrelation among the sources in the two groups,<sup>6</sup> they appear clearly distinguished on the  $E_{\text{cut}}-L_X$  plane. The sources in Branch 1 are: Her X-1, 4U 0115+63, Cen X-3, 4U 1626-67, 4U 1907+09, 4U 1538-522, GX 301-2, Cep X-4, IGR J16393-4643, IGR J16318-4848, and V0332+54. The sources in Branch 2 are: Vela X-1, XTE J1946+274, 1A 1118-61, 4U 0114+65, GX 304-1, OAO 1657-415, 4U 1700-37, GRO J1008-57, 4U 1909+07, 4U 2206+54, SW J2000.6+3210, SMC X-1, EXO 2030+375, 4U 1822-37, KS 1947+300, IGR J16207-5129, IGR J17544-2619, and IGR J18410-0535. Given that the nature of companion stars among the two lists is mixed (see table 1 of Sidoli & Paizis 2019), we see that this bi-modal behaviour cannot be distinguished on the basis of their companion (Be XRBs or supergiants) as illustrated in the Corbet diagram<sup>7</sup> for the X-ray pulsars in our study in Fig. 2.

Since we find only three sources with  $E_{\text{cut}}$  within the range of 7–14 keV, there appears to be a paucity of sources with  $E_{\text{cut}}$  around 10 keV, which is the same energy range where there is a gap between the XIS and PIN energy band. We therefore checked if this distribution is an artefact of the energy ranges considered here by simulating several fake spectra with varying cut-off energies distribute from 4–20 keV and fitting them. For all these fake spectra, we recovered the same spectral parameters as the input model thereby validating the robustness of our results.

Additionally, since the cut-off energies in the second group are spread around 6 keV, and most of the sources exhibit an iron emission line around 6.4 keV, there may be concerns about a possible mix-up between the iron line and cut-off energies for these sources. However, it should be noted that since the iron line emission in these sources are narrow features and prominently stand out in the X-ray emission, we can easily disentangle<sup>8</sup> between iron line and continuum parameters for a CCD spectrum. We also cross-checked this by simulating several fake spectra with varying cut-off energies (3–7 keV) and narrow iron lines of different equivalent width and were able to fully recover the input parameters, hence supporting our claim. Furthermore, there is no correlation between the cut-off energy and the iron line parameters as seen in the confidence plots for the iron line energy versus the cut-off energy, and the iron line normalization versus the cut-off energy for this group in Figs A1 and A2 in the Appendix.

In order to test the bi-modality against reported values in literature, we also checked the cut-off energy in literature (with RXTE) obtained using the same model as in this work. These values are tabulated in Table 5. We make a histogram of these literature values and the ones we obtain from our work and find that although for some sources, the cut-off energy is different in these two instruments, an apparent bi-modality is visible in both the cut-off energy distribution as seen in top panel of Fig. 3. It should be pointed out that we do not expect a one-to-one correspondence on the values of cut-off energies

<sup>6</sup>Note that we did not use A 0535+026, LMC X-4, and GX 1+4 in this plot, as  $E_{\text{cut}}$  for these three sources is obtained from the NPEX, FDCUT, and NEWHCUT models, respectively. All these models are mathematically different from HIGHECUT and thus the measured value of  $E_{\text{cut}}$  has a different meaning.

<sup>7</sup>[https://www.sternwarte.uni-erlangen.de/wiki/index.php/List\\_of\\_accreting\\_X-ray\\_pulsars](https://www.sternwarte.uni-erlangen.de/wiki/index.php/List_of_accreting_X-ray_pulsars)

<sup>8</sup>If the equivalent width of the iron line is smaller, it only gives large uncertainty for the line flux but does not affect the continuum parameters

**Table 2.** Parameters of the continuum and absorption features. Errors quoted are for 90 per cent confidence range.

Source	$N_{\text{H1}}^a$	$N_{\text{H2}}^a$	$C_V$	$\Gamma$	$\Gamma_{\text{norm}}^b$	$E_{\text{cut}}$ (keV)	$E_{\text{fold}}$ (keV)	$E_{\text{C1}}$ (keV)	$D_1$	$W_1$ (keV)	bb (kT)	$bb_{\text{norm}}^c$	$\chi^2_{\text{red}}/\text{dof}$
Her X-1	0.02	–	–	$0.81^{+0.02}_{-0.01}$	$0.084^{+0.004}_{-0.002}$	$19.47^{+0.16}_{-0.14}$	$12.34^{+0.35}_{-0.34}$	$38.14^{+0.33}_{-0.34}$	$0.98^{+0.08}_{-0.07}$	7	$0.55^{+0.02}_{-0.03}$	$0.00077^{+0.00001}_{-0.00001}$	1.55/661
4U 0115+63	$1.13^{+0.02}_{-0.02}$	–	–	$0.19^{+0.03}_{-0.02}$	$0.025^{+0.001}_{-0.002}$	$12.54^{+0.16}_{-0.18}$	$7.53^{+0.39}_{-0.25}$	9.57	0.67	1.0	$0.59^{0.01}_{0.01}$ $0.0012^{+0.0001}_{-0.0001}$	1.44/436	
Cen X-3	$1.43^{+0.03}_{-0.02}$	–	–	$1.09^{+0.01}_{-0.01}$	$0.392^{+0.089}_{-0.079}$	$15.14^{+0.17}_{-0.15}$	$8.07^{+0.37}_{-0.31}$	$28.66^{+0.82}_{-0.84}$	$0.28^{+0.09}_{-0.09}$	$5.41^{+2.42}_{-2.03}$	$0.107^{+0.006}_{-0.006}$	$0.049^{+0.015}_{-0.011}$	1.34/658
4U 1626-67	$0.09^{+0.02}_{-0.02}$	–	–	$0.830^{+0.008}_{-0.008}$	$0.0092^{+0.0001}_{-0.0001}$	$18.87^{+0.47}_{-0.44}$	$15.92^{+2.51}_{-1.85}$	$36.31^{+0.74}_{-0.64}$	$1.73^{+0.35}_{-0.28}$	$4.56^{+1.54}_{-1.25}$	$0.28^{+0.01}_{-0.01}$	$0.00014^{+0.00002}_{-0.00002}$	1.29/910
XTE 1946+274	$1.37^{+0.03}_{-0.03}$	$7.00^{+1.11}_{-1.01}$	$0.25^{+0.04}_{-0.04}$	$1.09^{+0.03}_{-0.04}$	$0.018^{+0.001}_{-0.001}$	$6.89^{+0.40}_{-0.52}$	$33.28^{+3.87}_{-4.28}$	$36.88^{+1.30}_{-1.18}$	$1.83^{+0.27}_{-0.26}$	7.5	–	–	1.12/816
Vela X-1	$1.29^{+0.03}_{-0.04}$	$3.02^{+0.20}_{-0.21}$	$0.43^{+0.02}_{-0.03}$	$1.16^{+0.02}_{-0.02}$	$0.19^{+0.01}_{-0.01}$	$5.53^{+0.15}_{-0.23}$	$35.79^{+3.15}_{-2.64}$	$27.90^{+0.57}_{-0.66}$	$0.102^{+0.025}_{-0.023}$	5.37	–	–	1.64/664
4U 1907+09	$2.47^{+0.06}_{-0.08}$	$2.81^{+0.86}_{-0.78}$	$0.24^{+0.08}_{-0.06}$	$1.29^{+0.01}_{-0.02}$	$0.0240^{+0.0004}_{-0.0008}$	$15.71^{+0.22}_{-0.27}$	$14.96^{+1.46}_{-2.15}$	$18.74^{+0.45}_{-0.39}$	$0.49^{+0.13}_{-0.19}$	$1.00^{+0.99}_{-1.00}$	–	–	1.07/882
4U 1538-522	$1.47^{+0.01}_{-0.01}$	–	–	$1.208^{+0.007}_{-0.008}$	$0.0506^{+0.0005}_{-0.0006}$	$15.94^{+1.26}_{-0.79}$	$14.29^{+0.86}_{-1.02}$	$21.46^{+0.43}_{-0.45}$	$0.53^{+0.11}_{-0.08}$	$2.09^{+0.76}_{-0.74}$	–	–	1.22/710
GX 301-2	$14.98^{+0.72}_{-0.73}$	$53.02^{+1.91}_{-1.97}$	0.95	$1.055^{+0.053}_{-0.058}$	$0.068^{+0.010}_{-0.009}$	$21.54^{+1.45}_{-1.25}$	$22.93^{+4.16}_{-3.40}$	$44.20^{+4.25}_{-3.40}$	$1.97^{+0.82}_{-0.52}$	19	–	–	1.11/529
1A 1118-61	$0.74^{+0.01}_{-0.01}$	–	–	$0.36^{+0.01}_{-0.01}$	$0.069^{+0.001}_{-0.001}$	$5.58^{+0.10}_{-0.09}$	$19.92^{+0.61}_{-0.57}$	$49.94^{+0.56}_{-0.51}$	$1.59^{+0.06}_{-0.06}$	$18.69^{+1.22}_{-1.16}$	–	–	1.61/468
4U 0114+65	$4.79^{+0.16}_{-0.22}$	$23.15^{+15.61}_{-9.85}$	$0.12^{+0.05}_{-0.04}$	$0.78^{+0.06}_{-0.06}$	$0.011^{+0.001}_{-0.001}$	$5.94^{+0.22}_{-0.24}$	$19.17^{+1.62}_{-1.72}$	$24.53^{+2.21}_{-2.71}$	$0.14^{+0.05}_{-0.06}$	5	$0.138^{+0.007}_{-0.006}$	$0.0180^{+0.0093}_{-0.0070}$	1.17/453
GX 304-1	$1.19^{+0.02}_{-0.01}$	$12.19^{+0.88}_{-0.78}$	$0.28^{+0.02}_{-0.02}$	$1.02^{+0.02}_{-0.03}$	$0.816^{+0.04}_{-0.04}$	$6.68^{+0.17}_{-0.20}$	$30.55^{+2.37}_{-2.04}$	$56.54^{+2.28}_{-1.54}$	$2.03^{+0.29}_{-0.18}$	$19.06^{+2.78}_{-2.18}$	–	–	1.39/673
OAO 1657-415	$16.67^{+0.54}_{-0.58}$	$43.06^{+5.00}_{-4.56}$	$0.45^{+0.03}_{-0.03}$	$0.49^{+0.04}_{-0.04}$	$0.011^{+0.001}_{-0.001}$	$6.14^{+0.14}_{-0.16}$	$16.18^{+0.67}_{-0.62}$	–	–	–	–	–	1.31/420
Cep X-4	$0.79^{+0.02}_{-0.02}$	$90.15^{+59.39}_{-30.79}$	$0.29^{+0.43}_{-0.07}$	$1.04^{+0.03}_{-0.03}$	$0.11^{+0.08}_{-0.01}$	$16.36^{+0.37}_{-0.58}$	$9.82^{+0.66}_{-0.58}$	$29.78^{+0.30}_{-0.30}$	$1.03^{+0.10}_{-0.09}$	$5.70^{+1.04}_{-0.90}$	$1.04^{+0.08}_{-0.06}$	$0.0011^{+0.0003}_{-0.0003}$	1.28/234
4U 1700-37	$2.03^{+0.04}_{-0.04}$	$4.43^{+0.11}_{-0.10}$	$0.70^{+0.01}_{-0.01}$	$0.94^{+0.01}_{-0.01}$	$0.184^{+0.005}_{-0.004}$	$6.48^{+0.05}_{-0.07}$	$19.93^{+0.39}_{-0.17}$	$37.38^{+1.77}_{-1.59}$	$0.09^{+0.01}_{-0.02}$	8	–	–	1.45/654
A0535+026 <sup>a</sup>	$0.74^{+0.07}_{-0.04}$	$5.50^{+0.86}_{-0.64}$	$0.35^{+0.04}_{-0.05}$	$1.14^{+0.09}_{-0.05}$	$0.048^{+0.005}_{-0.003}$	$13.15^{+4.06}_{-1.42}$	–	$41.91^{+1.02}_{-0.75}$	$10.14^{+3.83}_{-1.99}$	$1.43^{+0.37}_{-0.20}$	$0.089^{+0.013}_{-0.015}$	$0.0029^{+0.0044}_{-0.0012}$	1.09/706
4U 1822-37	0.1	–	–	$0.058^{+0.040}_{-0.037}$	$0.0131^{+0.0005}_{-0.0004}$	$3.10^{+0.14}_{-0.11}$	$7.16^{+0.39}_{-0.31}$	$35.41^{+8.55}_{-3.06}$	$0.39^{+0.66}_{-0.21}$	$4.11^{+9.27}_{-4.10}$	$0.189^{+0.007}_{-0.008}$	$0.0003^{+1.08845e-05}_{-1.06427e-05}$	1.24/477
GX J+4 <sup>phic</sup>	$14.52^{+0.43}_{-0.59}$	$25.06^{+7.21}_{-6.26}$	$0.24^{+0.06}_{-0.04}$	$1.265^{+0.021}_{-0.018}$	$0.110^{+0.007}_{-0.005}$	$23.94^{+1.23}_{-1.01}$	$41.63^{+1.04}_{-2.71}$	–	–	–	–	–	1.65/519
GRO J1008-57**	$1.35^{+0.09}_{-0.08}$	$6.15^{+0.94}_{-0.70}$	$0.34^{+0.03}_{-0.03}$	$1.10^{+0.02}_{-0.02}$	$0.129^{+0.006}_{-0.005}$	$6.39^{+0.16}_{-0.14}$	$22.79^{+0.79}_{-0.32}$	–	–	–	$0.127^{+0.02}_{-0.03}$	–	1.44/680
4U 1909+07	$6.45^{+0.45}_{-0.38}$	–	–	$1.06^{+0.08}_{-0.07}$	$0.0196^{+0.003}_{-0.002}$	$5.68^{+0.44}_{-0.27}$	$18.87^{+2.25}_{-1.61}$	–	–	–	–	–	1.27/288
IGR J16393-4643	$26.28^{+0.75}_{-0.74}$	–	–	$0.906^{+0.044}_{-0.046}$	$0.0036^{+0.0004}_{-0.0004}$	$19.72^{+1.19}_{-1.14}$	$10.37^{+1.62}_{-1.58}$	–	–	–	–	–	1.22/282
4U 2206+54	$0.40^{+0.04}_{-0.04}$	$1.41^{+0.19}_{-0.18}$	$0.59^{+0.04}_{-0.03}$	$1.34^{+0.07}_{-0.07}$	$0.041^{+0.004}_{-0.004}$	$3.43^{+0.26}_{-0.18}$	$25.85^{+4.32}_{-3.29}$	–	–	–	$1.98^{+0.05}_{-0.04}$	$0.0024^{+0.0001}_{-0.0001}$	1.39/665

Table 2 – continued

Source	$N_{\text{H1}}^a$	$N_{\text{H2}}^a$	$C_V$	$\Gamma$	$\Gamma_{\text{nom}}^b$	$E_{\text{cut}}$ (keV)	$E_{\text{fold}}$ (keV)	$E_{\text{C1}}$ (keV)	$D_1$	$W_1$ (keV)	bb (kT)	$bb_{\text{norm}}^c$	$\chi^2_{\text{red}}/\text{dof}$
SW	$1.41^{+0.17}_{-0.14}$	–	–	$0.92^{+0.28}_{-0.24}$	$0.0010^{+0.0013}_{-0.0010}$	$5.18^{+0.38}_{-0.50}$	$15.78^{+7.82}_{-5.08}$	–	–	–	$1.34^{+0.29}_{-0.22}$	$0.00022^{+0.00007}_{-0.00009}$	1.16/780
J2000.6+3210	0.1	$52.49^{+8.78}_{-7.76}$	$0.31^{+0.06}_{-0.07}$	$0.78^{+0.08}_{-0.08}$	$0.016^{+0.003}_{-0.003}$	$25.83^{+1.13}_{-2.78}$	$8.79^{+0.83}_{-0.78}$	–	–	–	$0.27^{+0.07}_{-0.09}$	–	1.23/382
LMC X-4	0.367 $^{+0.003}_{-0.003}$	$7.39^{+0.10}_{-0.67}$	$0.96^{+0.96}_{-0.21}$	$0.743^{+0.024}_{-0.001}$	$0.151^{+0.009}_{-0.004}$	$4.92^{+0.06}_{-0.06}$	$20.30^{+0.08}_{-0.35}$	–	–	–	$0.695^{+0.001}_{-0.012}$	$0.00015^{+0.00021}_{-0.00003}$	1.19/461
KS 1947+300	$1.99^{+0.01}_{-0.01}$	$65.08^{+4.35}_{-3.89}$	$0.22^{+0.01}_{-0.01}$	$1.37^{+0.02}_{-0.02}$	$0.641^{+0.024}_{-0.023}$	$7.28^{+0.13}_{-0.13}$	$21.69^{+0.38}_{-0.37}$	–	–	–	–	$0.017^{+0.00062}_{-0.00004}$	1.35/452
EXO 2030+375	0.05	–	–	$0.50^{+0.02}_{-0.03}$	$0.0102^{+0.0003}_{-0.0004}$	$4.80^{+0.16}_{-0.23}$	$10.31^{+0.25}_{-0.27}$	–	–	–	$0.178^{+0.028}_{-0.041}$	–	1.17/477
SMC X-1	$1.46^{+0.16}_{-0.15}$	–	–	$1.06^{+0.09}_{-0.08}$	$0.0006^{+0.0001}_{-0.0001}$	$22.12^{+1.53}_{-1.32}$	0.06	–	–	–	–	$0.00012^{+0.00010}_{-0.00004}$	1.13/193
V 0332+53	$7.64^{+0.54}_{-0.52}$	–	–	$1.43^{+0.09}_{-0.08}$	–	–	–	–	–	–	–	–	1.26/259
IGR J16493-4348	$122.43^{+3.88}_{-4.37}$	–	–	$1.03^{+0.08}_{-0.09}$	$0.0034^{+0.0006}_{-0.0005}$	$15.28^{+1.47}_{-1.69}$	$32.47^{+4.09}_{-3.59}$	–	–	–	–	–	1.26/223
IGRJ16318-4848	$12.38^{+1.01}_{-0.62}$	–	–	$1.34^{+0.12}_{-0.37}$	$0.009^{+0.003}_{-0.002}$	$7.16^{+5.84}_{-2.01}$	$35.63^{+18.95}_{-12.21}$	–	–	–	–	–	0.99/297
IGRJ16207-5129	$1.74^{+0.15}_{-0.15}$	$4.69^{+0.62}_{-0.55}$	$0.68^{+0.04}_{-0.05}$	$1.57^{+0.08}_{-0.08}$	$0.0128^{+0.0020}_{-0.0007}$	$5.06^{+0.72}_{-0.52}$	$56.39^{+31.77}_{-14.64}$	–	–	–	–	–	1.07/554
IGR J18410-0535	$1.39^{+0.07}_{-0.08}$	$2.43^{+0.28}_{-0.26}$	$0.60^{+0.05}_{-0.04}$	$1.29^{+0.02}_{-0.02}$	$0.0081^{+0.0004}_{-0.0004}$	$8.83^{+1.22}_{-1.09}$	$13.61^{+1.62}_{-1.54}$	–	–	–	–	–	1.07/496
IGR J17544-2619	$8.50^{+0.39}_{-0.38}$	–	–	$1.24^{+0.06}_{-0.06}$	$0.0031^{+0.0003}_{-0.0003}$	–	–	–	–	–	–	–	1.20/697
IGR J16195-4945	$1.81^{+0.32}_{-0.30}$	$5.83^{+1.26}_{-1.06}$	$0.78^{+0.06}_{-0.07}$	$2.20^{+0.15}_{-0.14}$	$0.0064^{+0.0022}_{-0.0015}$	–	–	–	–	–	–	–	1.03/695
IGR J16465-4507	$2.01^{+1.72}_{-0.33}$	$5.77^{+0.40}_{-0.86}$	$0.94^{+0.04}_{-0.18}$	$1.44^{+0.08}_{-0.05}$	$0.0032^{+0.0005}_{-0.0003}$	–	–	–	–	–	–	–	0.85/150
IGR J16479-4514	$1.39^{+0.52}_{-0.61}$	$4.26^{+1.43}_{-1.16}$	$0.82^{+0.09}_{-0.13}$	$2.05^{+0.19}_{-0.19}$	$0.0019^{+0.0008}_{-0.0006}$	–	–	–	–	–	–	–	0.89/211
IGR J17391-3021	0.1	$4.02^{+0.88}_{-0.81}$	$0.80^{+0.05}_{-0.06}$	$2.48^{+0.18}_{-0.18}$	$0.0012^{+0.0004}_{-0.0003}$	–	–	–	–	–	–	–	1.22/504
IGR J08408-4503	$0.93^{+0.19}_{-0.21}$	$3.43^{+1.61}_{-1.11}$	$0.75^{+0.05}_{-0.07}$	$2.79^{+0.28}_{-0.21}$	$0.0029^{+0.0018}_{-0.0009}$	–	–	–	–	–	–	–	0.96/521
IGR J00370+6122	–	–	–	–	–	–	–	–	–	–	–	–	–

Notes. <sup>a</sup> In units of  $10^{22}$  atoms  $\text{cm}^{-2}$ ;

<sup>b</sup> In units of photons  $\text{keV}^{-1} \text{cm}^{-2} \text{s}^{-1}$  at 1 keV;

<sup>c</sup> In units of  $L_{39}/D_{10}$ , where  $D_{10}$  is the distance to the source in units of 10 kpc.

\* The cyclotron line features are at 10 keV, an energy range that is not covered by *Suzaku* data.

\*\* The cyclotron line feature is at 86 keV, i.e. beyond the energy range covered by *Suzaku* data in this paper.

<sup>f</sup> Here FDCUT is used, <sup>n</sup> NPEX is used, <sup>he</sup> NEWHCUT is used with width = 20 keV.

**Table 3.** Cyclotron line harmonics detected in a few sources among those used in this paper.

Source	$E_{C1}$ (keV)	$D_1$	$W_1$ (keV)	$E_{C2}$ (keV)	$D_2$	$W_2$ (keV)
4U 0115+63	$17.89^{+0.12}_{-0.13}$	$0.68 \pm 0.01$	$6.03^{+0.27}_{-0.28}$	$30.48^{+1.27}_{-1.21}$	$0.29 \pm 0.04$	7
Vela X-1	$51.42^{+0.71}_{-0.63}$	$2.13^{+0.19}_{-0.18}$	10.5	–	–	–
4U 1538-522	52	10	$1.18^{+1.09}_{-0.82}$	–	–	–
4U 0114+65	$36.45^{+3.20}_{-3.84}$	$0.25^{+0.14}_{-0.13}$	5	–	–	–

from these two instruments since they cover different energy ranges and also because for some sources, the X-ray spectrum evolve with flux (see Reig & Nespoli 2013). The interesting finding here is the apparent bi-modal distribution of cut-off energy for sources even within the same class.

We also carried out a number of statistical tests to quantify the bi-modality in the distribution of cut-off energy so obtained. We first performed a 2D KS test<sup>9</sup> for these two branches. The 2D test allow us to compare how different the two distributions are from each other. For the  $L_X$  versus  $E_{\text{cut}}$  variation for red and green groups, the  $p$  value is low ( $\sim 1 \times 10^{-5}$ ) indicating that these two distributions are different.

However, since our main finding is the bi-modality in the distribution of cut-off energy, we next focus on this. We performed a Dip test<sup>10</sup> (Hartigan & Hartigan 1985) and obtained a  $p$ -value of 0.15. The rule of thumb for interpretation of this test is that  $p$ -values less than 0.05 indicate significant bimodality and values in the range of 0.05–0.10 suggest bimodality with marginal significance. Therefore, while the Dip test do not favour multimodality in the cut-off energy, it should be remarked that this Hartigan’s Dip test work best for small samples but with large bumps.<sup>11</sup> The alternative approach is therefore to search for modes in the data distribution by generating the probability densities<sup>12</sup> of the cut-off energies. In order to do this, we first calculate the best value of band-width based on Silverman’s band-width test and then look for points of inflexion in the Kernel (probability) Density Estimates (KDE) using this band-width as the smoothing function. As seen in the middle of Fig. 3, we find two points of inflexion at  $\sim 5.7$  and 17.8 keV. In the same plot, we have also overplotted the probability density of histogram using the bin size as the band-width to demonstrate bi-modality.

Finally, we also fit the frequency estimate obtained from histogram with a single Gaussian and two Gaussian functions. As seen from the lower panel of Fig. 3, the histogram is better described by a two Gaussian function ( $\chi_{\text{red}}^2 \sim 0.7$ ) and a single Gaussian simply fail to fit and result in large ( $>30$ ) values of  $\chi_{\text{red}}^2$ .

Next, we extracted the PIN pulse profiles (15.0–70.0 keV) for the pulsating sources in each branch to check if a different beaming mechanism (fan or pencil; Davidson & Ostriker 1973; Burnard, Arons & Klein 1991) could be at the origin of the observed bi-modality.<sup>13</sup> As shown in Fig. 4, the single and double peaked pulse profiles indicating pencil and fan beam, respectively, are spread out

in both groups at random. We therefore also conclude that the current bi-modality in the distribution between  $E_{\text{cut}}$  and  $L_X$  is not based on the beaming pattern of X-rays. As the beaming pattern depends on the accretion rate,  $\dot{M}$ , the bi-modality is independent of beaming pattern and the accretion rate as well. That the bi-modality in  $E_{\text{cut}}$  is independent of the X-ray luminosity (and hence the accretion rate), can also be seen from Fig. 1. We maintained the same colour scheme for the different sources in all other figures that we describe in the following sections to investigate alternative possibilities that could give rise to the observed behaviour.

We inspected the ratio of the source spectra to Crab to see if the  $E_{\text{cut}}$  values measured are also evident in the Crab spectral ratio. We however found that since CRSF is rather strong for many sources, the spectral curvature is affected by this absorption feature in the X-ray spectrum for many sources and bi-modality therefore is not straightforward to interpret from this exercise.

Furthermore, in order to check the robustness of our results, with another model, we also tried fitting the 29 sources (that required a cut-off energy) with another phenomenological model ‘FDCUT’ in XSPEC. We could reasonably fit 26 sources with FDCUT, albeit with much higher reduced chi-square than HIGHECUT for each source. We find that even when fitting with FDCUT, there are two branches distinguished in the  $L_X$  versus  $E_{\text{cut}}$  plane – similar to what we see with HIGHECUT. Note, however that since the cut-off energies for both these models are mathematically different from each other, their numerical values do not match.

All these factors indicate that the bi-modality in the X-ray spectral shape of these groups are possibly real and further investigations with physical models will allow us to further understand the cause for this. Such detailed studies is however beyond the scope of this work.

#### 4.1.2 $\Gamma$ versus $L_X$

We report the dependence of  $\Gamma$  as a function of  $L_X$  in the case of neutron star HMXBs (including Be XRBs, SGXBs, SFXTs, and a few LMXBs), accreting high magnetic field NS in LMXBs spanning over five orders of magnitude in X-ray luminosity. As we show in top of Fig. 5, we find that for all these sources  $\Gamma$  and  $L_X$  are marginally anticorrelated with the best fit to all our data as:  $\Gamma = a \log L_{X33} + b$ , where  $a = -0.25 \pm 0.04$ ,  $b = 1.93 \pm 0.15$ . The dependence of  $\Gamma$  as a function of  $L_X$  in the case of Be XRBs have been previously investigated by Reig & Nespoli (2013) who found that  $\Gamma$  and  $L_X$  anticorrelate with the X-ray flux during the low X-ray intensity (sub-critical) states of these sources, while a positive correlation is measured during the high intensity (supercritical) states. Their study spanned two orders of magnitude variation in  $L_X$ .

It should be noted that most of the sources in our sample are in the sub-critical luminosity regime (see Section 5) and our findings are therefore consistent with the anticorrelation seen by Reig & Nespoli (2013) for individual sources.

<sup>9</sup><https://github.com/syrte/ndtest/blob/master/ndtest.py>

<sup>10</sup><https://github.com/BenjaminDoran/unidip>

<sup>11</sup><https://www.paspk.org/wp-content/uploads/2019/11/9-ES-609A-Comparison-of-Modality.pdf>

<sup>12</sup><https://towardsdatascience.com/modality-tests-and-kernel-density-estimations-3f349bb9e595>

<sup>13</sup>We did not extract the pulse profiles of the two sources 4U 1822-37, due to the very low pulse fraction (see Sasano et al. 2014), and V 0332+53, due to the limited statistics of the available *Suzaku* data.

**Table 4.** Emission lines detected in the sources present in this paper.

Source	EL (keV)	EQ (keV)	EL (keV)	EQ (keV)	EL (keV)	EQ (keV)	EL (keV)	$\sigma$ (keV)
Her X-1	$6.51^{+0.04}_{-0.05}$	$0.23^{+0.005}_{-0.005}$	$6.65^{+0.02}_{-0.02}$	$0.056^{+0.005}_{-0.005}$	$6.40^{+0.18}_{-0.01}$	$0.031^{+0.003}_{-0.003}$	$0.90^{+0.02}_{-0.02}$ 1.06	$0.198^{+0.014}_{-0.016}$ $0.300^{+0.054}_{-0.054}$
4U 0115+63	$6.65^{+0.08}_{-0.06}$	$0.06^{+0.02}_{-0.02}$	–	–	–	–	–	–
Cen X-3	$6.409^{+0.006}_{-0.005}$	$0.070^{+0.003}_{-0.003}$	$6.658^{+0.009}_{-0.009}$	$0.047^{+0.003}_{-0.003}$	$6.977^{+0.018}_{-0.018}$	$0.038^{+0.003}_{-0.002}$	–	–
4U 1626-67	$6.70^{+0.09}_{-0.09}$	$0.029^{+0.003}_{-0.003}$	–	–	–	–	$0.913^{+0.005}_{-0.004}$ 1.015 <sup>+0.002</sup> <sub>-0.001</sub>	$0.03^{+0.01}_{-0.01}$ 0.009
XTE 1946+274	$6.43^{+0.02}_{-0.02}$	$0.025^{+0.004}_{-0.004}$	–	–	–	–	–	–
Vela X-1	$6.403^{+0.001}_{-0.003}$	$0.054^{+0.002}_{-0.002}$	$7.09^{+0.02}_{-0.03}$	$0.0075^{+0.001}_{-0.001}$	–	–	$0.904^{+0.006}_{-0.008}$ 1.361 <sup>+0.007</sup> <sub>-0.007</sub>	1.83E-05 2.15E – 05
4U 1907+09	$6.393^{+0.006}_{-0.004}$	$0.061^{+0.005}_{-0.005}$	$7.01^{+0.04}_{-0.03}$	$0.0091^{+0.0007}_{-0.0007}$	–	–	–	–
4U 1528-522	$6.417^{+0.007}_{-0.005}$	$0.067^{+0.004}_{-0.004}$	–	–	–	–	–	–
GX 301-2	$6.378^{+0.005}_{-0.003}$	$0.216^{+0.008}_{-0.008}$	–	–	–	–	$2.95^{+0.03}_{-0.03}$	1.67E-05
1A 1118-61	$6.399^{+0.005}_{-0.004}$	$0.053^{+0.003}_{-0.003}$	$7.07^{+0.03}_{-0.03}$	$0.010^{+0.003}_{-0.003}$	–	–	–	–
4U 0114+65	$6.42^{+0.01}_{-0.01}$	$0.029^{+0.003}_{-0.003}$	$7.09^{+0.03}_{-0.04}$	$0.012^{+0.001}_{-0.001}$	–	–	–	–
GX 304-1	$6.46^{+0.01}_{-0.01}$	$0.034^{+0.003}_{-0.003}$	–	–	–	–	–	–
OAO 1657-415	$6.461^{+0.001}_{-0.003}$	$0.252^{+0.006}_{-0.006}$	$7.130^{+0.009}_{-0.008}$	$0.094^{+0.002}_{-0.002}$	–	–	–	–
Cep X-4	$6.46^{+0.02}_{-0.03}$	$0.322^{+0.006}_{-0.006}$	–	–	–	–	–	–
4U 1700-37	$6.419^{+0.003}_{-0.003}$	$0.073^{+0.001}_{-0.001}$	$7.09^{+0.01}_{-0.01}$	$0.014^{+0.001}_{-0.001}$	–	–	–	–
A0535+026	$6.40^{+0.02}_{-0.02}$	$0.0232^{+0.005}_{-0.005}$	–	–	–	–	–	–
4U 1822-37	$6.41^{+0.01}_{-0.01}$	$0.082^{+0.008}_{-0.008}$	$6.97^{+0.03}_{-0.03}$	$0.025^{+0.006}_{-0.006}$	–	–	–	–
GX 1+4	$6.42^{+0.003}_{-0.003}$	$0.144^{+0.001}_{-0.001}$	$7.09^{+0.01}_{-0.01}$	$0.028^{+0.003}_{-0.003}$	$7.46^{+0.04}_{-0.04}$	$0.061^{+0.007}_{-0.007}$	–	–
GRO J1008-57	$6.39^{+0.01}_{-0.01}$	$0.016^{+0.001}_{-0.001}$	$7.07^{+0.06}_{-0.06}$	$0.0033^{+0.0003}_{-0.0003}$	–	–	–	–
4U 1909+07	$6.416^{+0.008}_{-0.009}$	$0.0713^{+0.005}_{-0.005}$	–	–	–	–	–	–
IGR J16393-4643	$6.36^{+0.03}_{-0.02}$	$0.039^{+0.008}_{-0.008}$	–	–	–	–	–	–
4U 2206+54	6.4	$0.007^{+0.004}_{-0.004}$	–	–	–	–	–	–
SW J2000.6+3210	$6.29^{+0.07}_{-0.06}$	$0.019^{+0.007}_{-0.006}$	–	–	–	–	–	–
LMC X-4	$6.49^{+0.03}_{-0.03}$	$0.056^{+0.011}_{-0.011}$	–	–	–	–	$0.69^{+0.15}_{-0.12}$	$0.23^{+0.05}_{-0.09}$
KS 1947+300	$6.51^{+0.03}_{-0.03}$	$0.033^{+0.004}_{-0.004}$	$7.30^{+0.07}_{-0.07}$	$0.022^{+0.003}_{-0.003}$	–	–	–	–
EXO 2030+375	$6.38^{+0.0}_{-0.0}$	$0.021^{+0.002}_{-0.002}$	$6.64^{+0.0}_{-0.0}$	$0.019^{+0.001}_{-0.001}$	–	–	2.5 3.26 <sup>+0.03</sup> <sub>-0.03</sub>	$0.12^{+0.04}_{-0.04}$ 4.8E-02
SMC X-1	$6.32^{+0.03}_{-0.03}$	$0.030^{+0.009}_{-0.009}$	$5.89^{+0.16}_{-0.17}$	$0.025^{+0.011}_{-0.010}$	–	–	$1.30^{+0.05}_{-0.03}$ 0.88 <sup>+0.02</sup> <sub>-0.01</sub>	$0.08^{+0.08}_{-0.08}$ $0.00018^{+0.00008}_{-0.00009}$
V 0332+53	–	–	–	–	–	–	–	–
IGR J16493-4348	$6.49^{+0.05}_{-0.07}$	$0.034^{+0.015}_{-0.015}$	–	–	–	–	–	–
IGRJ16318-4848	$6.39^{+0.02}_{-0.02}$	$0.698^{+0.048}_{-0.050}$	$7.11^{+0.01}_{-0.02}$	$0.153^{+0.011}_{-0.011}$	$7.44^{+0.05}_{-0.05}$	$0.079^{+0.006}_{-0.006}$	–	–
IGRJ16207-5129	$6.40^{+0.03}_{-0.03}$	$0.038^{+0.010}_{-0.013}$	–	–	–	–	–	–
IGR J18410-0535	$6.38^{+0.03}_{-0.03}$	$0.032^{+0.008}_{-0.008}$	–	–	–	–	–	–
IGR J17544-2619	$6.38^{+0.03}_{-0.02}$	$0.015^{+0.005}_{-0.005}$	–	–	–	–	–	–
IGR J16195-4945	$6.39^{+0.03}_{-0.03}$	$0.039^{+0.020}_{-0.016}$	–	–	–	–	–	–
IGR J16465-4507	6.4	0.001	–	–	–	–	–	–
IGR J16479-4514	$6.36^{+0.04}_{-0.04}$	$0.053^{+0.002}_{-0.002}$	–	–	–	–	–	–
IGR J17391-3021	–	–	–	–	–	–	–	–
IGR J08408-4503	–	–	–	–	–	–	–	–
IGR J00370+6122	–	–	–	–	–	–	–	–

The luminosity span in this work is however much larger than the RXTE observation of Reig & Nespoli (2013) and while the RXTE observations focused on the evolution of spectra for individual sources (using multiple observations of same Be XRB pulsars at different luminosities), we focus on the overall ‘class’ behaviour of the sources as a function of luminosity. Another improvement with the previous paper is that for the RXTE observations, the authors

froze the  $N_H$  values for most of the sources while in our analysis – given the better low energy coverage of XIS – we were able to constrain both the photon index and the  $N_H$  independently (see contour plots, Figs A3 and A4 in Appendix) in most cases.<sup>14</sup>

<sup>14</sup>except some systems where the line of sight absorption is very low, like LMC X-4, Her X-1, SMC X-1 etc; see Table 2



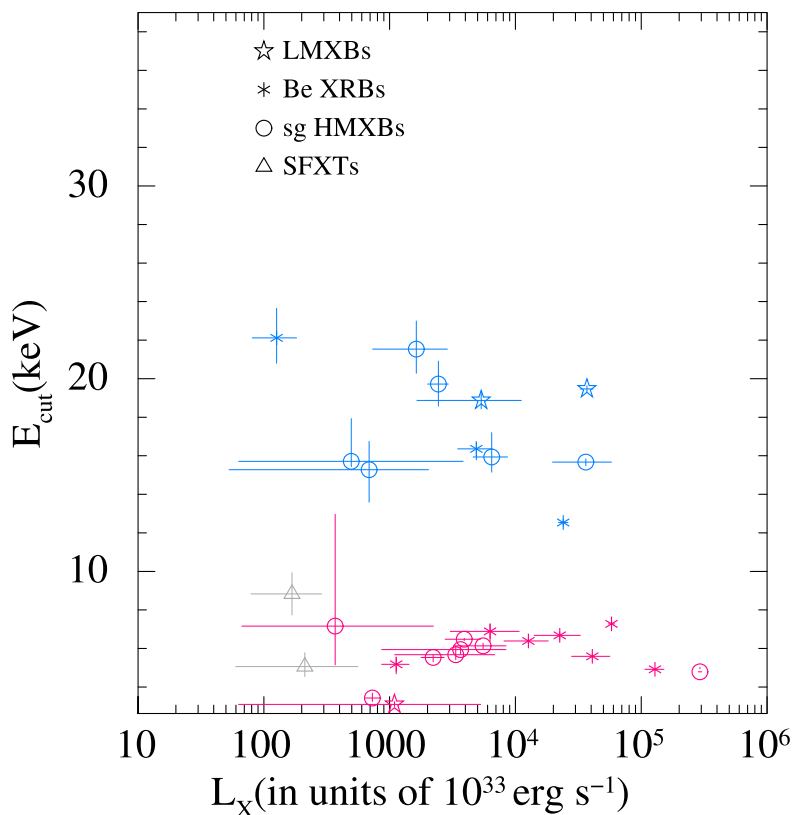


**Figure 1.** Plot of cut-off energy versus the X-ray luminosity. To identify the apparent dichotomy, we mark the two groups in blue and magenta with SFXTs marked in grey.

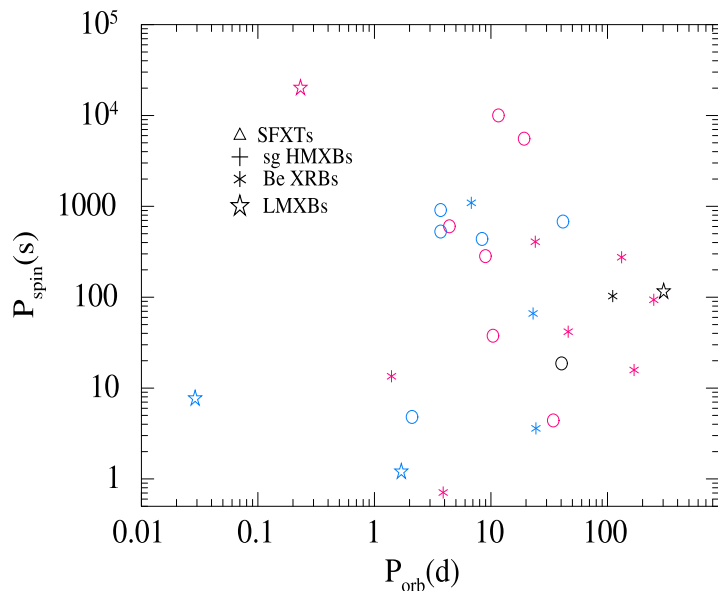


**Figure 2.** Corbet diagram of the pulsars in our study. Sources marked in blue and magenta are for the sources with cut-off energy greater than and less than 10 keV, respectively. As seen in the plot, the distinction is not on the basis of the companion star being a Be X-ray binary or an OB star.

#### 4.1.3 $E_{\text{fold}}$ versus $L_X$

In models of the X-ray spectrum,  $E_{\text{fold}}$  is a measure of the electron temperature of the infalling plasma. An anticorrelation between luminosity and  $E_{\text{fold}}$  has been reported earlier for individual sources like A 0535+26, RX J0440.9+4431, for example (Ferrigno et al. 2013; Müller et al. 2013). It is for the first time that we present

here a comprehensive behaviour of the  $E_{\text{fold}}$  dependence on  $L_X$  using a wider sample. In the bottom panel of Fig. 5, we see that with increasing luminosity, the  $E_{\text{fold}}$  value show a weak anticorrelation with the Pearson co-efficient<sup>15</sup> for these two quantities being  $-0.19$ .

<sup>15</sup><https://www.socscistatistics.com/tests/pearson/>

**Table 5.** Literature values of cut-off energies from RXTE data. To maintain consistency with the cut-off energy measurements, we take these values from the same instrument.

Source	$E_{\text{cut}}$	Positive error	Negative error	Ref
Her X-1	22	1.4	0.8	(Coburn et al. 2002)
4U 0115+6	10	0.5	0.4	(Coburn et al. 2002)
Cen X-3	21.3	0.2	0.4	(Coburn et al. 2002)
4U 1626-67	6.8	0.3	0.3	(Coburn et al. 2002)
XTE J1946+274	22	0.8	0.9	(Coburn et al. 2002)
Vela X-1	17.9	0.3	0.4	(Coburn et al. 2002)
4U 1907+09	13.5	0.2	0.2	(Coburn et al. 2002)
4U 1538-52	13.57	0.04	0.05	(Coburn et al. 2002)
GX 301-2	17.3	0.1	0.2	(Coburn et al. 2002)
1A 1118-61	5.88	0.17	0.19	(Devasia et al. 2011)
GX 304-1	6.08	0.16	0.19	(Rothschild et al. 2017)
Cep X-4	16.3	0.1	0.1	(Koyama et al. 1991)
4U 1909+07	7.8	0.5	0.5	(Fürst et al. 2011)
KS 1947+300	6.5	0.5	0.5	(Tsygankov & Lutovinov 2005)
	15.8	0.5	0.5	(Tsygankov & Lutovinov 2005)
4U 2206+54	7.3	0.1	0.1	(Corbet & Peele 2001)
EXO 2030+375	7.7	0.2	0.2	(Epili et al. 2017)
SMC X-1	13.7	3.4	3.4	(Inam, Baykal & Beklen 2010)
	6.6	1.6	1.6	(Inam et al. 2010)

#### 4.1.4 $E_{\text{fold}}$ versus $E_{\text{cut}}$

We find that the sources in Branch 2 (magenta) have a somewhat larger median of  $E_{\text{fold}}$  than those in Branch 1 (blue). A plot of their variation is shown in Fig. 6. We remark here that we could independently constrain both the  $E_{\text{cut}}$  and  $E_{\text{fold}}$  as seen in the confidence plots in Appendix (Figs A5 and A6) and there is no degeneracy between these two quantities for both groups.

A similar correlation between these two quantities has also been reported earlier by Makishima et al. 1999 where the cut-off energies seem to be divided into two groups (their Fig. 12b) less than and above 10 keV. The authors however do not comment about this in their paper.

#### 4.1.5 $E_{\text{cut}}$ versus $E_{\text{cyc}}$

The variation of  $E_{\text{cut}}$  with  $E_{\text{cyc}}$  for HMXBs has been investigated in earlier works. Coburn et al. (2002) and Makishima et al. (1999) used *RXTE* and *Ginga* data, respectively, to obtain the relationship  $E_{\text{cut}} \propto E_{\text{cyc}}^{0.7}$  for  $E_{\text{cyc}}$  below 35 keV. Thanks to the broad-band spectral capability of *Suzaku*, in our analysis, we show that the correlation between these two quantities (contour plots in Fig. A7 in Appendix) is not unique but rather have a complex behaviour (left-hand panel of Fig. 7). The sources in blue branch can be fitted to a functional form of  $E_{\text{cut}} \propto E_{\text{cyc}}^{0.82 \pm 0.08}$  (marked by the black line). The functional form for sources in magenta is  $E_{\text{cut}} \propto E_{\text{cyc}}^{0.29 \pm 0.06}$  (black dashed line). In order to make a comparison with the latest result, we digitized the graph<sup>16</sup> in Staubert (2003) to fit their Fig. 8 and find that in their work, they report:  $E_{\text{cut}} \propto E_{\text{cyc}}^{0.47(-0.35, 0.39)}$  which is consistent with our results for both groups within errors.

It should however be noted that if we allow for an offset, we get a different best fit result of  $E_{\text{cut}} = 8 + E_{\text{cyc}}^{0.67}$  and  $E_{\text{cut}} = 5 \times E_{\text{cyc}}^{0.36}$ . Therefore, while various forms work in the correlation between these quantities and the correlation is not mathematically unique, it is evident visually that the blue branch does have a steeper slope in this graph. We also remark here that the values of  $E_{\text{cyc}}$  we obtain

from this work are close to values obtained in Coburn et al. (2002). The difference between the fig. 9 of Coburn et al. (2002) and Fig. 7 of this work is a result of the determination of the values of  $E_{\text{cut}}$  which is possibly not surprising since we do not expect a one-to-one correspondence on the values of cut-off energies from RXTE and *Suzaku* as they cover different energy ranges and also because for some sources, the X-ray spectrum evolve with flux (see Reig & Nespoli 2013).

#### 4.1.6 CRSF width $W_c$ versus $E_{\text{cyc}}$

The variation of the CRSF width versus  $E_{\text{cyc}}$  is shown on the right-hand side of Fig. 7. In agreement with the results of Coburn et al. (2002) and Staubert et al. (2019), we observe a linear correlation between the two quantities. We are aware that using a HIGHECUT model can sometimes lead to artificial widening of the CRSF energy if  $E_{\text{cyc}}$  and  $E_{\text{cut}}$  are close to each other. To mitigate this, we took great care in constraining the width of the CRSF properly and cross-checked the values with those available in literature. For example, the three sources (1A 1118-61, GX 301-2, and GX 304-1), where we obtain large widths are consistent with their literature values (Suchy et al. 2012, 2011; Jaisawal, Naik & Epili 2016). From our fits of the broad-band data, we find  $W_c \propto E_{\text{cyc}}^{(2.2 \pm 0.5)}$ . Overall, as we see from Table 2 and in Fig. 8 that the higher the value of cyclotron line energy, the deeper the line is.

#### 4.1.7 $Fe K\alpha$ flux versus continuum flux

From Fig. 9, we see that the *Suzaku* data of the considered sources suggest a strong correlation between the continuum flux and the Fe  $K\alpha$  flux. Such a correlation<sup>17</sup> is expected and was also previously reported by Giménez-García et al. (2015) and Torrejón et al. (2010) but over a smaller range of continuum flux.

<sup>17</sup>We remark here that all spectra used for the current analysis were cumulated outside X-ray eclipses.

<sup>16</sup><https://www.digitizeit.de>

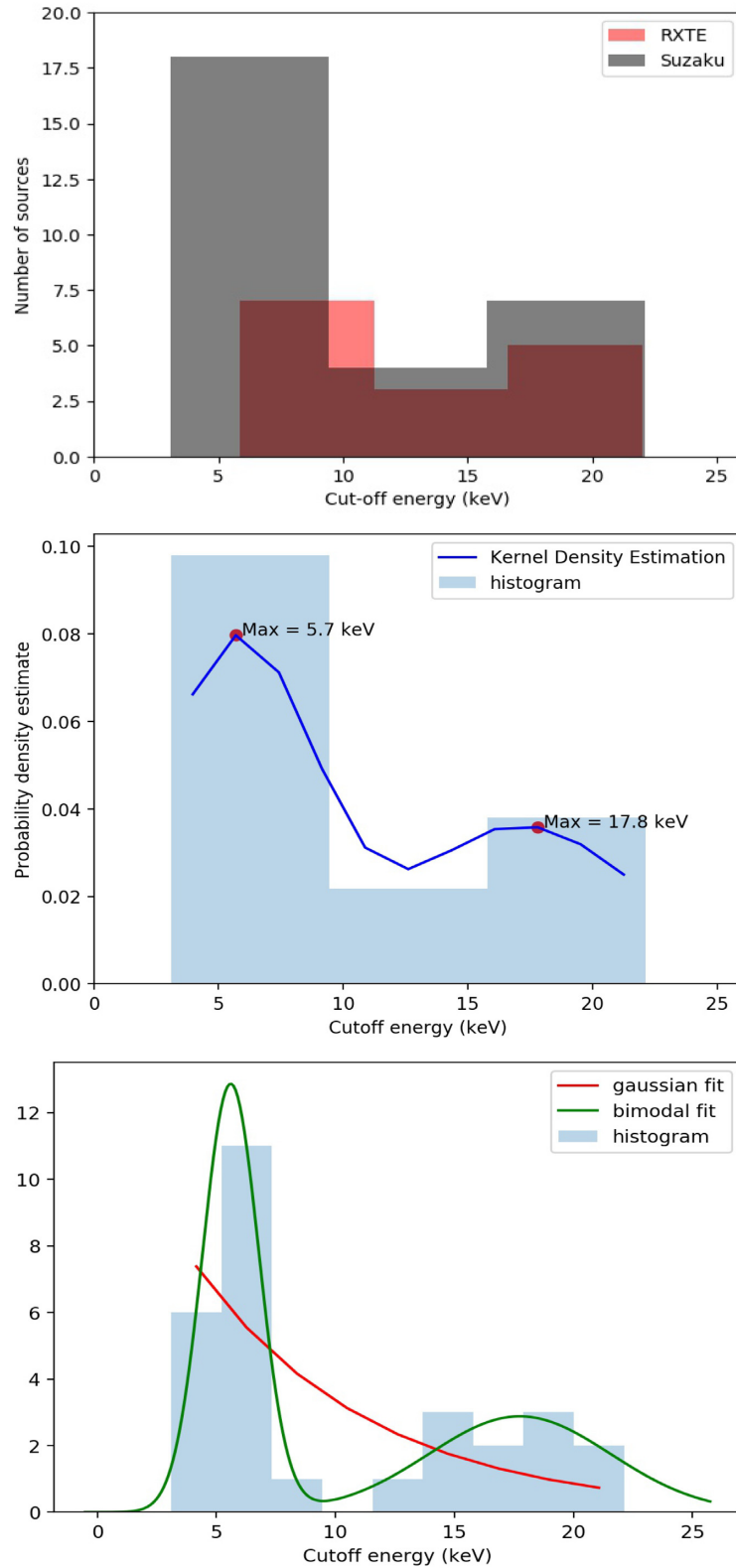


**Figure 3.** Top: Histogram of cut-off energies from RXTE in red and the current work in grey. The RXTE measurements are indicative of the bi-modality as found in the *Suzaku* measurements. Middle: The KDE plotted (with a chosen Silverman bandwidth of 3) demonstrate that there are two peaks in the data at  $\sim 5.7$  keV and  $\sim 17.8$  keV respectively. Bottom: The shaded blue region is the histogram for *Suzaku* data with finer binning compared to top and middle figure. The histogram fits well with a bi-modal function plotted in green as compared to single Gaussian fits shown by red line (the trailing edge of Gaussian).

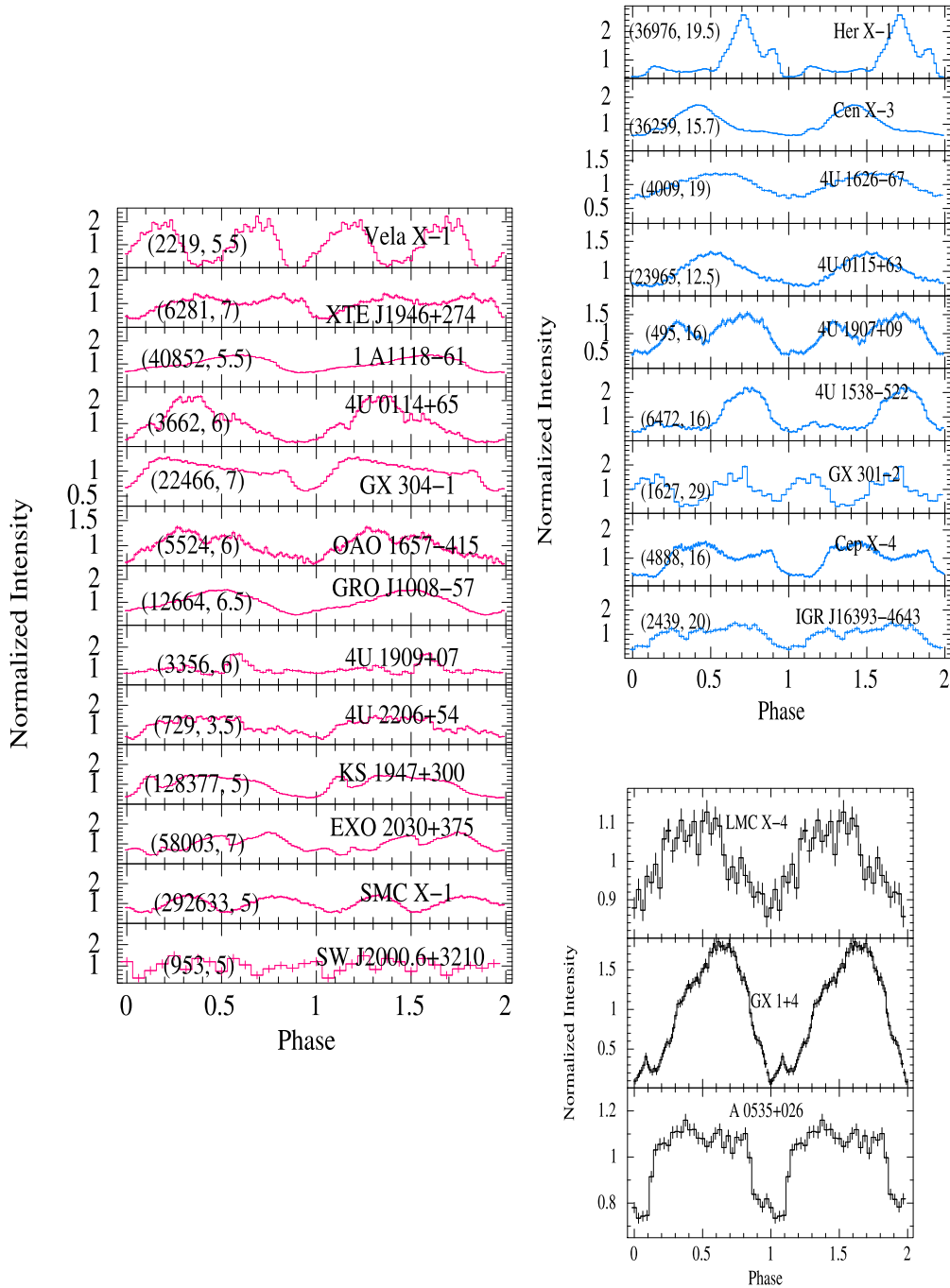


**Figure 4.** Left-hand panel: HXD-PIN (15–70 keV) pulse profiles of pulsars in the magenta branch. Right-hand panel (top): HXD-PIN (15–70 keV) pulse profiles of pulsars in the blue branch. The first number in parenthesis in both the figures is the X-ray luminosity in units of  $10^{33} \text{ erg s}^{-1}$  and the second number is the cut-off energy in keV. Right-hand panel (bottom): Pulse profiles for three sources, LMC X-4, GX 1+4 and A 0535+026 which could not be fit with the HIGHECUT model. See the text for details.

#### 4.1.8 Equivalent width (EW) of $K\alpha$ iron line versus $L_x$

On the right-hand side of Fig. 9, we show the lack of any clear correlation between the equivalent width of the iron  $K\alpha$  line and the source X-ray luminosity. An anticorrelation between these two parameters have been reported earlier in the literature by Giménez-García et al. (2015), Vasylenko, Zhdanov & Fedorova (2015), and Torrejón et al. (2010). This anticorrelation is usually interpreted in terms of the so-called Baldwin effect (Baldwin 1977). As previous studies were carried out in a limited energy range, we checked that

our results did not change when only the XIS data are used to fit the spectra (with a power law corrected for photoelectric line-of-sight absorption and Gaussian) of all the sources (0.8–10 keV). We also performed the same study by using the restricted energy range 7.1–12.0 keV to estimate the X-ray luminosity of each source (only photons above 7.1 keV contribute to the  $K\alpha$  emission and the photoelectric cross-section drops rapidly so that photons above 12 keV do not contribute much in this process) and the energy range 4.95–7.75 keV as done in Torrejón et al. (2010). In none of these

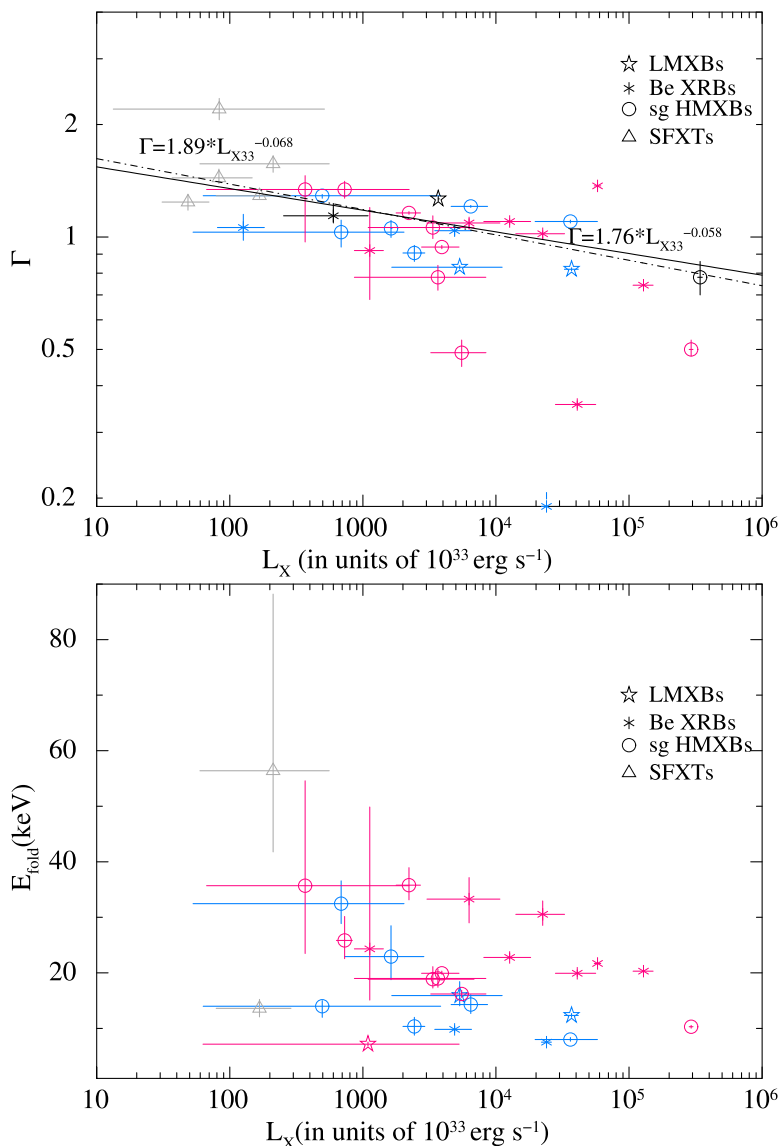


**Figure 5.** Top: Variation of photon index with luminosity. The black solid line represents the best fit to the data ( $\Gamma \propto L_X^{-\alpha}$  with  $\alpha = 0.058 \pm 0.006$  when sources fit with only XIS spectrum fits are excluded (see Section 3, third-last paragraph). The best fit to all the data points (marked in dotted line) is  $\alpha = 0.068 \pm 0.006$ . The sources A 0535+26, GX 1+4, and LMC X-4 have been marked in black. Bottom: The variation of  $E_{\text{fold}}$  energy with X-ray luminosity. Both the figures are marked with the same colour coding as in Fig. 1.

cases we could find a clear indication of the anticorrelation reported previously. In addition, we have also explored similar correlation using *XMM* data in a different work where we do not find any such relation between EW and luminosity (see fig. 2 of Pradhan, Bozzo & Paul 2018).

The existence of this X-ray Baldwin effect has been a matter of much debate for AGNs and possibly depend on different class of AGNs. A systematic analysis of many AGNs using *XMM* and *INTEGRAL* data showed a very weak correlation between the EW of Fe K  $\alpha$  line and luminosity (see Vasylenko et al. 2015 and references therein). We will return to this discussion in Section 5.

#### 4.1.9 Equivalent width (EW) of K $\alpha$ versus $N_H$

As visible from Fig. 10, we found a clear linear correlation between the hydrogen column density of the different sources and the

equivalent width of their K  $\alpha$  lines. Here  $N_H = N_{H1} + N_{H2} * C_V$ , where  $N_{H1}$  is the hydrogen column density along our line of sight to the source,  $N_{H2}$  accounts for local absorption and  $C_V$  is the covering fraction, the latter having a wide range of 0.1–0.96 (see Table 2).

Generally, it is well known that when a relatively limited energy range is used for the X-ray spectral fitting on data with limited statistical quality (e.g. 0.5–10.0 keV), the derived values of the absorption column density and the power-law spectral index can be positively correlated (a larger absorption column density can be used in such restricted energy range to fit the spectrum equally well with a steeper power law). We also checked a priori the variation of  $\Gamma$  as a function of  $N_H$  to cross-check some of our results and find that this is not the case for our spectral analysis, mainly thanks to the wide energy coverage of the instruments onboard *Suzaku* (see contour plots, Figs A3 and A4 in the Appendix).

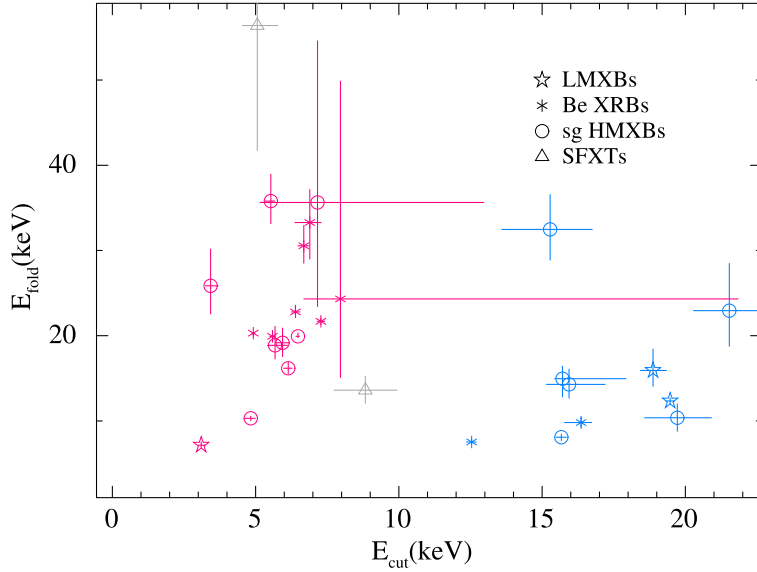


**Figure 6.** Variation of  $E_{\text{fold}}$  with  $E_{\text{cut}}$  marked with the same colour coding as in Fig. 1.

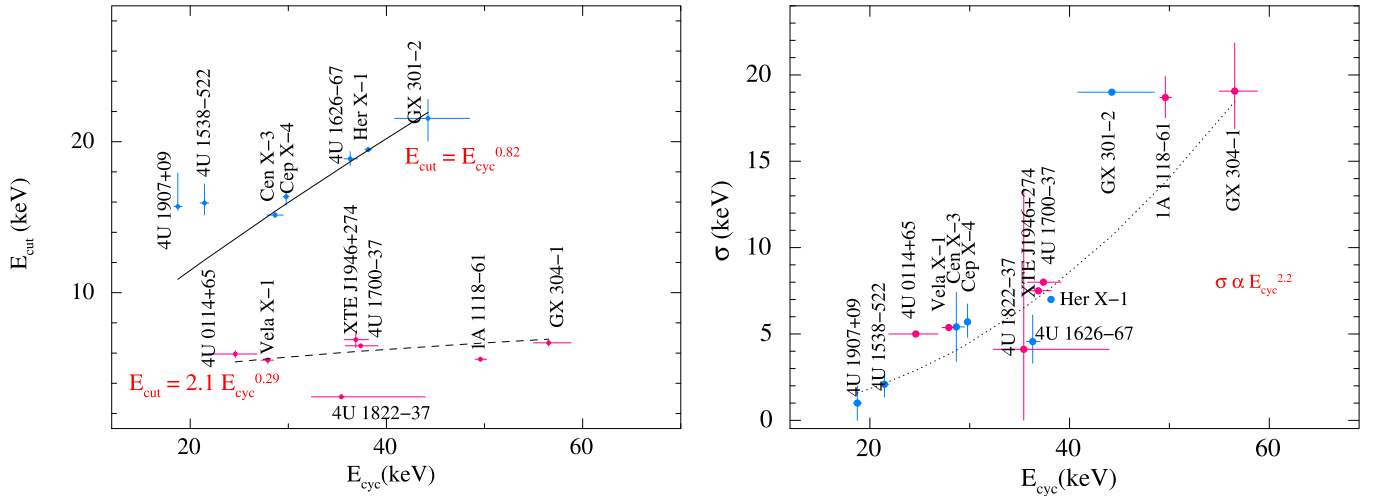


**Figure 7.** Left-hand panel:  $E_{\text{cut}}$  versus  $E_{\text{cyc}}$  showing two scaling laws for two groups. Right-hand panel: Positive correlation between CRSF width  $W_c$  versus  $E_{\text{cyc}}$ . All the figures are marked with the same colour coding as in Fig. 1.

## 5 DISCUSSION

In this paper, we took advantage of the broad energy coverage of the instruments onboard *Suzaku* to perform a systematic study of all observed neutron star HMXBs, including the high magnetic field LMXB pulsars displaying a cyclotron absorption line in their spectra. The aim of our analysis was to explore a number of correlations between the spectral parameters of these sources reported previously in the literature. We used for the analysis of all sources a similar spectral model, in order to carry out a consistent investigation of all their spectral parameters. While detailed individual studies of most of these sources are already reported in literature, our aim with this paper is to outline a comprehensive behaviour of HMXBs as a class. Such a study was last carried out nearly two decades back in early 2000s (Coburn et al. 2002).

We summarize the main results of the paper below:

(i) The broad-band X-ray spectra of all HMXBs that we considered in this paper can be described by a power-law component

modified by a cut-off energy (where PIN data are usable). This spectral shape is usually interpreted in terms of Comptonization of the seed photons produced in the thermal mound of the neutron star accretion column by free electrons in the accreting material. It is therefore expected that the spectral cut-off energies are proportional to the electron temperature.

A lack of correlation between  $E_{\text{cut}}$  and  $L_X$  has been reported earlier by White et al. (1983). They point out, however, that the low luminosity systems in their sample do exhibit a somewhat less sharp cut-offs at higher energies.

In this study, we found all analysed systems distributing on two different branches in the  $E_{\text{cut}}$  and  $L_X$  plot. For sources in Branch 1 (represented in blue in all plots), the cut-off energy, that is a measure of the electron temperature, vary from 12–24 keV and increases with the mass accretion rate (in turns regulating the X-ray luminosity). For sources following the Branch 2 (magenta),  $E_{\text{cut}}$  remains in a narrower range from 3–10 keV, even when  $L_X$  changes by a factor of  $\sim 1000$ . This result indicates that the cut-off energies of the

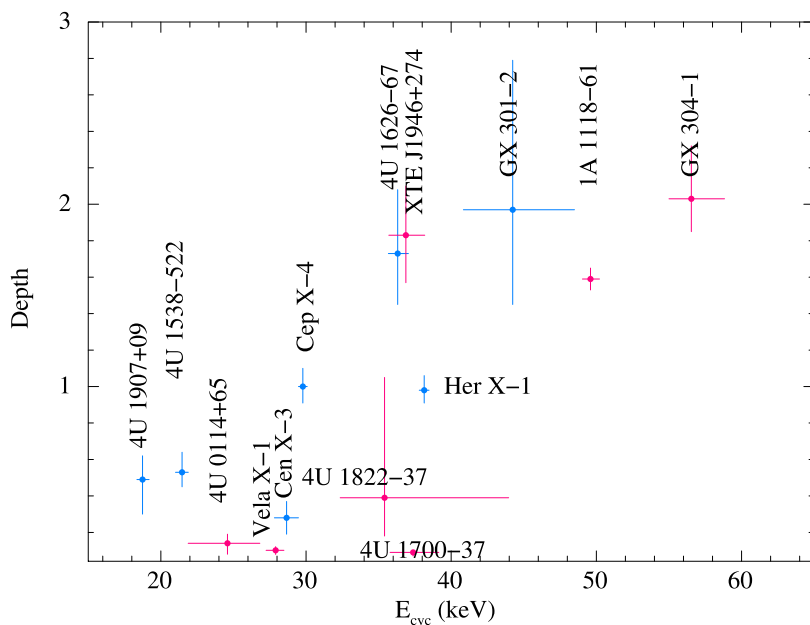


**Figure 8.** Plot of CRSF depth versus CRSF energy. All the figures are marked with the same colour coding as in Fig. 1.

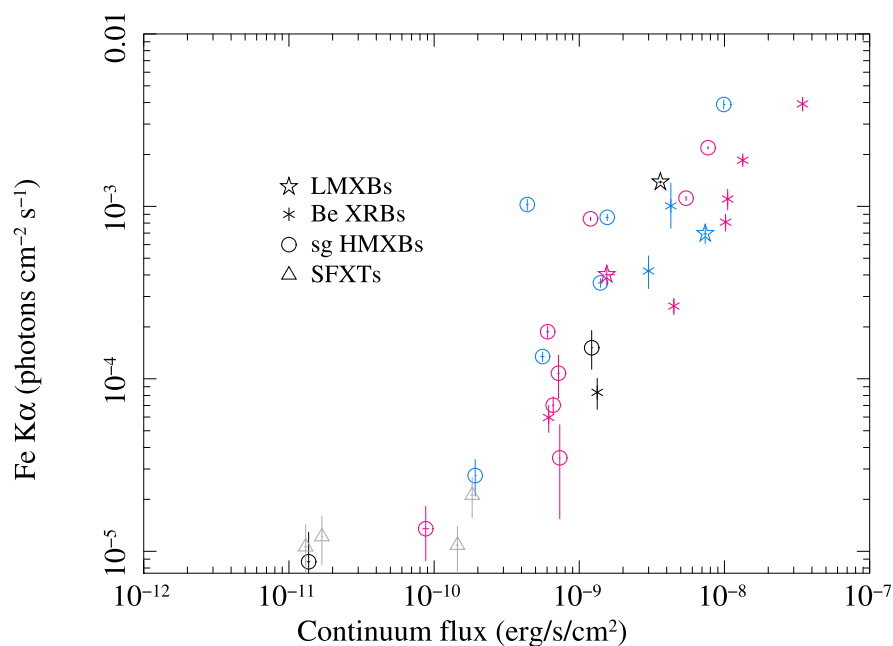


**Figure 9.** Plot of the iron line flux versus continuum flux marked with the same colour coding as in Fig. 1.

sources do not depend only on the luminosity. As we showed in Section 3, this different behaviour cannot either be simply ascribed to switches between a pencil and a fan beam emission geometry due to the lack of clear systematic variations in the pulse profiles of the analysed sources. To the best of our knowledge, so far, no theoretical explanation has been proposed in the literature to interpret this behaviour.

(ii) An anticorrelation between  $\Gamma$  and  $L_X$  is known to exist in neutron star LMXBs and black hole systems (for luminosities lower than ‘critical’ luminosity) where accretion takes place through a disc (Wu & Gu 2008; Allen et al. 2015). Wijnands et al. (2015) suggested that in case of strongly magnetized neutron stars the presence of

a magnetic field could significantly alter the spectra, such that a direct comparison between HMXBs and LMXBs is not possible. For this study, we make use of systems containing in all cases strongly magnetized neutron stars ( $B \gtrsim 10^{12}$  G) and accreting both from discs and from stellar winds. We found that the anticorrelation between  $\Gamma$  and  $L_X$  still holds, indicating that in HMXBs, the Comptonization process makes the spectrum harder at increasing  $L_X$  at least in the subcritical regime (even though it might break down at luminosities higher than  $10^{37}$  ergs  $s^{-1}$ ).

For black hole binaries, since this anticorrelation is valid for luminosities below a critical value, we also cross-checked the X-ray luminosity of each pulsar against the critical luminosity of each

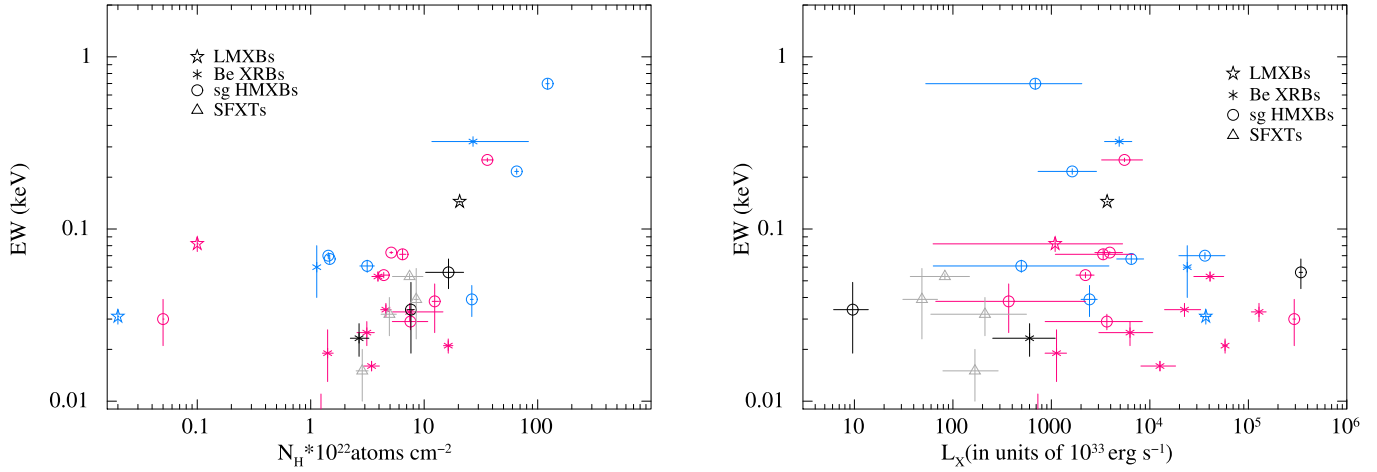


**Figure 10.** Left-hand panel: Plot of the equivalent width versus luminosity. Right-hand panel: Plot of absorption column density versus the EW of iron line. We use for all plots the same colour coding of Fig. 1.

pulsar using equation (3) (Becker et al. 2012) below.

$$L_{\text{crit}} = 1.49 \times 10^{37} \text{ erg s}^{-1} \times \left(\frac{\Lambda}{0.1}\right)^{-7/5} \times w^{-28/15} \times \left(\frac{M}{1.4 M_{\odot}}\right)^{29/30} \left(\frac{R}{10 \text{ km}}\right)^{1/10} \left(\frac{B_{\text{surf}}}{10^{12} \text{ G}}\right)^{16/15}, \quad (3)$$

where  $R$ ,  $M$ , and  $B$  are, the radius, mass, and surface magnetic field strength ( $B$  in terms of  $\sim 10^{12}$  G) of the neutron star,  $\Lambda = 1$ , and  $w = 1$  for wind-accreting systems. For all those sources with measured  $B$  (through CRSF line energy), we find that besides Her X-1, 4U 0115+63, Cen X-3, and 1A 1118-61, all other sources are indeed in the subcritical regime.

(iii) An anticorrelation of  $E_{\text{fold}}$  with  $L_X$  indicates that with increasing luminosity,  $E_{\text{fold}}$  (a proxy for electron temperature of the ‘infalling’ plasma) decreases. As the luminosity increases, the radiation field from the neutron star begin to affect the accretion flow and Compton cooling becomes more efficient (since scattering rate of photons off electrons increase). This leads to the shift of electron temperature towards lower energies with increasing luminosity giving rise to this anticorrelation of  $E_{\text{fold}}$  with  $L_X$ .

(iv) From the variation of folding energy with cut-off energies, we see that smaller cut-off energy imply larger folding energies. It has also been reported by earlier authors that the non-cyclotron-line pulsars should exhibit larger values of folding energy (less steep spectral breaks) due to their lack of the spectral trough caused by an absorption like feature in CRSF (Makishima et al. 1999). However, when we compared the folding energy of cyclotron line sources with the folding energy of non-cyclotron line sources, we see no such trend.

(v) The variation of  $E_{\text{cut}}$  with  $E_{\text{cyc}}$  has been studied in a number of earlier works (Makishima et al. 1990, 1999; Coburn et al. 2002). Makishima et al. (1990) obtained a linear correlation between  $E_{\text{cut}}$  and  $E_{\text{cyc}}$  ( $E_{\text{cut}} = 1.4\text{--}1.8 E_{\text{cyc}}$ ). From the measurements of  $E_{\text{cut}}$ , they thus inferred that the magnetic field of HMXBs was spanning a relatively narrow range ( $1\text{--}4 \times 10^{12}$  G). Nine years later, these results were updated by Makishima et al. (1999). These authors used a larger sample of sources to prove that there exists a saturation of  $E_{\text{cut}}$  at high values of  $E_{\text{cyc}}$  ( $E_{\text{cut}} \propto E_{\text{cyc}}^{0.7}$ ). They interpreted this finding by suggesting that the presence of a thermal emission component can affect the position of the spectral energy break. Coburn et al. (2002) reconfirmed the same relationship, adding also new constrains on

the saturation of  $E_{\text{cut}}$ . The latter seems to be detected only below 35 keV. They also suggested the possible presence of two linear relations between  $E_{\text{cut}}$  and  $E_{\text{cyc}}$ , one below 35 keV and one above. Our current study has an added advantage of the broad-band energy coverage compared to these previous works in literature. We find that for higher values of magnetic field, the cut-off energies tend to saturate for both these groups. This is possibly because there could be some other relativistic effects in the creation of the continuum that become important at higher values of magnetic field.

(vi) The right-hand panel of Fig. 7 shows that in this study we found a relatively well marked linear correlation between the energy of the cyclotron line and its width. Such a correlation is expected because the cyclotron line undergoes Doppler-broadening due to the thermal motion of electrons at temperature  $kT_e$  and was first noted by Trümper et al. (1977). There have been other comprehensive works agreeing with this phenomenon in recent years (e.g., Coburn et al. 2002, Staubert et al. 2019). The FWHM of a CRSF changes with the viewing angle  $\theta$  of the observer with respect to the magnetic field as follows - see footnote 11 on Staubert et al. (2020):

$$W_c \propto E_c \sqrt{kT_e} |\cos(\theta)| \quad (4)$$

This implies that two quantities, the characteristic electron temperature,  $kT_e$  and  $\theta$  (angle between the observer line of sight and the neutron star magnetic field) for all sources considered in this paper are not dramatically different. The linear correlation are also indicative of small values of  $kT_e$  as discussed in Coburn et al. (2002). The reason for this is that the matter being accreted on to the hot spots form an accretion column and in the steady state, the amount of matter falling in balances the matter spreading out at the base where the mound parameters (area, density etc) are similar for most sources irrespective of accretion rate. Our results support their argument since despite five orders of magnitude change in  $L_X$  in this work, our findings are indicative of the same linear correlation. Alternatively, this correlation can also be explained if the temperature is tied to the magnetic field strength as seen in some simulations of gamma-ray bursts (Lamb & Wasserman 1990).

Another implication of this relation is that, any effect of  $\theta$  is also very small. Since the bulk motion of the electrons (which in turn depend on the accretion rate) also play a role in line broadening, we should have expected this correlation to smear out. This brings us to a very interesting point as has been discussed in Coburn et al. (2002) that



accretion could have an influence on the relative orientation of spin and magnetic axes, with the spin axis presumably being influenced by the age of the system and the accretion time-scales making  $\theta$  very small. This correlation can be further tested for individual sources by detailed pulse profile modelling of each source and measuring the width of the CRSF line with varying  $\theta$ .

It is also interesting to mention here that in Staubert et al. (2019), there are two groups in width of CRSF versus energy (their Fig. 12) where the authors argue that the second slope are mostly consist of ‘outlier’ sources. We find similar scatter in the depth of CRSF versus CRSF energy (Fig. 8) although the sources do not hold a on-to-one correspondence in both the works.<sup>18</sup>

(vii) Our analysis also confirmed the presence of a strong correlation between the X-ray continuum of all the sources where a  $K\alpha$  iron emission line is found and the line flux. This is expected, since the Fe  $K\alpha$  line is thought to be produced in these systems due to the reprocessing of the X-ray continuum by iron atoms in the matter surrounding the neutron star (being either the material from the stellar winds in HMXBs or the disc in LMXBs). As was also discussed by Torrejón et al. (2010) and Giménez-García et al. (2015), we thus expect the Fe  $K\alpha$  line flux to increase with the flux of the continuum.

Historically, an inverse correlation was obtained between the EW of C IV lines and the UV luminosity in AGNs (Baldwin effect; Baldwin 1977). Analogously, correlation studies between the EW of  $K\alpha$  lines and  $L_X$  have been carried out for AGNs and XRBs providing indications for an inverse correlation (Torrejón et al. 2010; Giménez-García et al. 2015; Vasylenko et al. 2015). This anticorrelation between the EW of  $K\alpha$  lines and  $L_X$  is called the X-ray Baldwin Effect. At odds with the results of Giménez-García et al. (2015) and Torrejón et al. (2010), we did not detect any significant correlation between the EW of the Fe  $K\alpha$  lines and the source X-ray luminosity. As discussed by Torrejón et al. (2010), we noticed in our case that a marginal correlation (not statistically significant) is visible when the EW of the  $K\alpha$  line is plotted against the X-ray flux but the correlation disappears when the luminosity is used in place of the flux.

The non-confirmation of the X-ray Baldwin effect for the Fe  $K\alpha$  in X-ray binaries is probably not surprising since there is no physical reason for the effect to hold true for XRBs with the neutral iron line. In case of AGNs the physical reason for the anticorrelation of EW of C IV lines with luminosity is that for higher luminosity the atoms are highly ionized and do not produce C IV lines in same proportion. However, in the case of the neutral 6.4 keV iron line in X-rays, if the increase in luminosity cause the ionisation to be so high as to remove the K-shell electrons, we should be seeing the Hydrogen like and Helium like iron atoms and the iron line would instead be seen at 6.7 and 6.9 keV instead of the neutral  $K\alpha$  line at 6.4 keV. On the contrary, very few HMXBs like Cen X-3 (Naik et al. 2011), OAO 1657-415 (Pradhan, Raman & Paul 2019), for example, show these emission lines.

(viii) Finally, we also reported on the positive correlation between the EWs of the iron  $K\alpha$  line and the absorption column density local to the HMXB sources ( $N_H$ ). This correlation is expected because a larger  $N_H$  implies that more stellar wind material around the neutron star is involved in the formation of a stronger iron line (see e.g. Inoue 1985; Pradhan et al. 2014, 2015; Giménez-García et al. 2015; Pradhan et al. 2019) except in some sources with accretion disc like SMC X-1, where a relatively low column density is seen (Pradhan,

Maitra & Paul 2020). In others like the persistent Be XRB, SW J2000.6+3210, the iron line is almost undetectable since there is not enough matter surrounding the neutron star to facilitate fluorescence (Pradhan et al. 2013).

Although we have very few SFXTs compared to classical sg HMXBs in this work, we note that the absorption column density (and EW) for these SFXTs are smaller when compared to classical sgXBs (see Table 2). This motivated us to look into our findings with more details by including a larger sample of SFXTs. We also therefore extended this study by including *XMM* data and have discussed the findings in detail in Pradhan et al. (2018) which we refer to the reader for further details. We find that the lower  $N_H$  and lower EW should be expected for SFXTs. Such a difference is either due to faster (or rarer) stellar winds in SFXTs or due to the inhibition of accretion in SFXTs most of the time by other mechanisms like magnetic gating (Bozzo, Falanga & Stella 2008) leading to inefficient photoionization of the stellar wind.

We reported in the plots of Figs 9 and 10 also the LMXBs considered in this paper for completeness, but we do not expect them to follow a similar correlation as for the HMXBs. For LMXBs, the iron line is indeed supposed to have a completely different origin than in HMXBs (see e.g. Cackett & Miller 2013).

The residuals from all the best fits to the data of the different sources are shown in Figs 11 and 12 and various contour plots are shown in the Appendix.

## 6 SUMMARY

In this section, we summarize the main results of our work discussed above. This class analysis of the broad-band X-ray spectrum of 39 accreting neutron star X-ray binaries indicate some interesting findings. (i) We find that the relationship between the cut-off energy and X-ray luminosity follow a bi-modal behaviour. The interpretation of such a dichotomy is not straightforward and is not a result of different companion stars (LMXBs, Be XRBs, sgXBs) or beaming patterns (explored through pulse profiles). We encourage further studies using physical continuum and line models in order to investigate this behaviour. (ii) We also find that the dependence of cut-off energies on the CRSF energy is not unique. We also confirm the previous findings of Coburn et al. (2002) that the width (and depth) of the CRSF is linearly correlated to the CRSF energy. (iii) We confirm the correlation between the iron  $K\alpha$  emission line and the X-ray continuum flux, between the EW of the iron  $K\alpha$  line and absorption. This is expected since such lines are formed by the fluorescence of the X-ray continuum photons in interstellar matter around the NS in case of HMXBs. We also note that the EW and absorption are different between SFXTs and classical HMXBs and interpret that as being caused by difference in stellar wind properties between these two systems or a result of inhibited accretion in SFXTs during most times. Finally, (iv) we note that the photon index and  $E_{\text{fold}}$  is negatively correlated with luminosity, thus suggesting that Compton cooling becomes more efficient at higher luminosities which makes the spectrum harder and also lowers the electron temperature of the plasma.

Overall, we have updated the correlation between spectral parameters of accreting neutron stars taking advantage of the broad-band energy coverage of *Suzaku*. Such a study was long overdue in literature with the last such study made almost two decades back.

<sup>18</sup>Note that there is often a variation in CRSF parameters over different time and/or spin phases



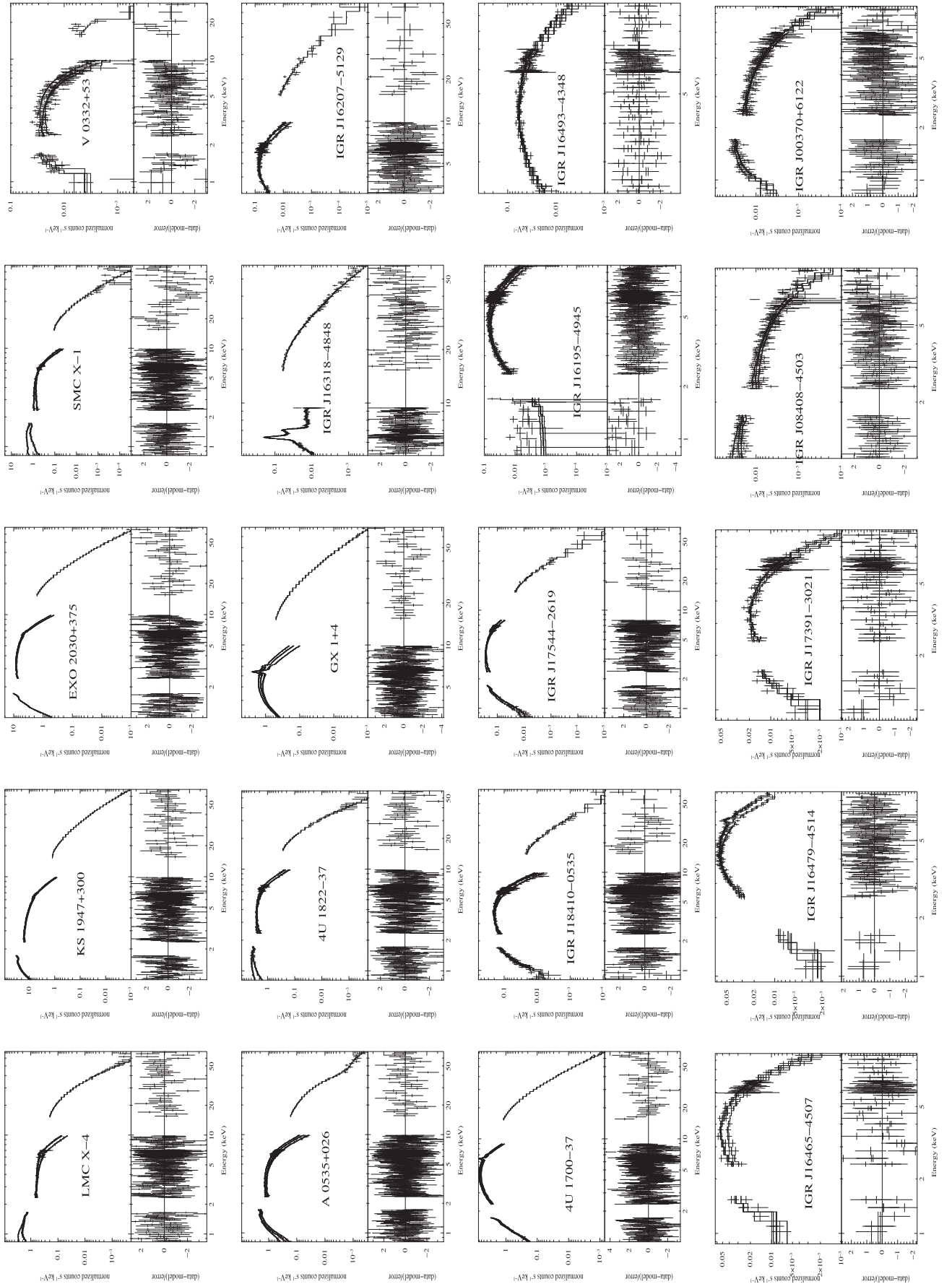


**Figure 12.** Spectra of all considered sources together with residuals from the best fits. All best-fitting results are reported in Table 2 contd.

## ACKNOWLEDGEMENTS

The authors would like to acknowledge the referee for his/her thorough and constructive comments that greatly improved the quality of the paper. PP would like to thank Raman Research Institute, Bengaluru and St Joseph's College, Darjeeling for the infrastructure facilities provided during the preparation of this work. PP would also like to thank Dipankar Bhattacharya for useful discussions and also the members of XMAG for their useful comments. Finally, PP would like to acknowledge the grant received as a part of Minor Research Project from University Grants Commission, India that partly supported this work. This research has made use of data and/or software provided by the High Energy Astrophysics Science Archive Research Center (HEASARC), which is a service of the Astrophysics Science Division at NASA/GSFC.

## DATA AVAILABILITY

The data underlying this article will be shared on reasonable request to the corresponding author.

## REFERENCES

- Allen J. L., Linares M., Homan J., Chakrabarty D., 2015, *ApJ*, 801, 10
- Baldwin J. A., 1977, *ApJ*, 214, 679
- Barragán L., Wilms J., Pottschmidt K., Nowak M. A., Kreykenbohm I., Walter R., Tomsick J. A., 2009, *A&A*, 508, 1275
- Basko M. M., Sunyaev R. A., 1975, *A&A*, 42, 311
- Becker P. A., Wolff M. T., 2007, *ApJ*, 654, 435
- Becker P. A. et al., 2012, *A&A*, 544, A123
- Bildsten L. et al., 1997, *ApJS*, 113, 367
- Bodaghee A., Tomsick J. A., Rodriguez J., Chaty S., Pottschmidt K., Walter R., Romano P., 2011, *ApJ*, 727, 59
- Bonnet-Bidaud J. M., Mouchet M., 1998, *A&A*, 332, L9
- Bozzo E., Falanga M., Stella L., 2008, *ApJ*, 683, 1031
- Burderi L., Di Salvo T., Robba N. R., La Barbera A., Guainazzi M., 2000, *ApJ*, 530, 429
- Burnard D. J., Arons J., Klein R. I., 1991, *ApJ*, 367, 575
- Cackett E. M., Miller J. M., 2013, *ApJ*, 777, 47
- Chakrabarty D., 1998, *ApJ*, 492, 342
- Chakrabarty D., Roche P., 1997, *ApJ*, 489, 254
- Chakrabarty D., Wang Z., Juett A. M., Lee J. C., Roche P., 2002, *ApJ*, 573, 789
- Chaty S., Rahoui F., Foellmi C., Tomsick J. A., Rodriguez J., Walter R., 2008, *A&A*, 484, 783
- Coburn W., Heindl W. A., Rothschild R. E., Gruber D. E., Kreykenbohm I., Wilms J., Kretschmar P., Staubert R., 2002, *ApJ*, 580, 394
- Coe M. J. et al., 1994, *MNRAS*, 270, L57
- Corbet R. H. D., Peele A. G., 2001, *ApJ*, 562, 936
- Davidson K., Ostriker J. P., 1973, *ApJ*, 179, 585
- Devasia J., James M., Paul B., Indulekha K., 2011, *MNRAS*, 414, 1023
- Epili P., Naik S., Jaisawal G. K., Gupta S., 2017, *MNRAS*, 472, 3455
- Ferrigno C., Farinelli R., Bozzo E., Pottschmidt K., Klochov D., Kretschmar P., 2013, *A&A*, 553, A103
- Filliatre P., Chaty S., 2004, *ApJ*, 616, 469
- Fukazawa Y. et al., 2009, *PASJ*, 61, 17
- Fürst F., Kreykenbohm I., Suchy S., Barragán L., Wilms J., Rothschild R. E., Pottschmidt K., 2011, *A&A*, 525, A73
- Giménez-García A., Torrejón J. M., Eikmann W., Martínez-Núñez S., Oskinova L. M., Rodes-Roca J. J., Bernabéu G., 2015, *A&A*, 576, A108
- Hartigan J. A., Hartigan P. M., 1985, *Ann. Stat.*, 13, 70
- Hemphill P. B., Rothschild R. E., Markowitz A., Fürst F., Pottschmidt K., Wilms J., 2014, *ApJ*, 792, 14
- Heras J. A. Z., Walter R., 2004, *Astron. Telegram*, 336, 1
- Hill A. B., Dean A. J., Landi R., McBride V. A., de Rosa A., Bird A. J., Bazzano A., Sguera V., 2008, *MNRAS*, 385, 423
- Hung L.-W., Hickox R. C., Boroson B. S., Vrtilik S. D., 2010, *ApJ*, 720, 1202
- Inam S. Ç., Baykal A., Beklen E., 2010, *MNRAS*, 403, 378
- Inoue H., 1985, *Space Sci. Rev.*, 40, 317
- Jaisawal G. K., Naik S., Epili P., 2016, *MNRAS*, 457, 2749
- Kaper L., van der Meer A., Najarro F., 2006, *A&A*, 457, 595
- Koyama K. et al., 1991, *ApJ*, 366, L19
- Koyama K. et al., 2007, *PASJ*, 59, 23
- Kühnel M. B. n. et al., 2020, *A&A*, 634, A99
- Lamb D. Q., Wang J. C. L., Wasserman I. M., 1990, *ApJ*, 363, 670
- Maitra C., Paul B., 2013a, *ApJ*, 771, 96
- Maitra C., Paul B., 2013b, *ApJ*, 763, 79
- Makishima K. et al., 1990, *ApJ*, 365, L59
- Makishima K., Mihara T., Nagase F., Tanaka Y., 1999, *ApJ*, 525, 978
- Masetti N., Bassani L., Bazzano A., Dean A. J., Stephen J. B., Walter R., 2006, *Astron. Telegram*, 815, 1
- Masetti N. et al., 2008, *A&A*, 482, 113
- Mason K. O., Cordova F. A., 1982, *ApJ*, 262, 253
- Megier A., Strobel A., Galazutdinov G. A., Krelowski J., 2009, *A&A*, 507, 833
- Mihara T., 1995, PhD thesis, Dept. of Physics, Univ. of Tokyo (M95)
- Mitsuda K. et al., 2007, *PASJ*, 59, 1
- Morel T., Grosdidier Y., 2005, *MNRAS*, 356, 665
- Müller D., Klochov D., Caballero I., Santangelo A., 2013, *A&A*, 552, A81
- Nagase F., 1989, *PASJ*, 41, 1
- Naik S., Paul B., Ali Z., 2011, *ApJ*, 737, 79
- Negueruela I., Roche P., Fabregat J., Coe M. J., 1999, *MNRAS*, 307, 695
- Nielsen J., Hickox R. C., Vrtilik S. D., 2004, *ApJ*, 616, L135
- Nespoli E., Fabregat J., Mennickent R. E., 2008, *A&A*, 486, 911
- Parkes G. E., Murdin P. G., Mason K. O., 1980, *MNRAS*, 190, 537
- Pellizza L. J., Chaty S., Negueruela I., 2006, *A&A*, 455, 653
- Pradhan P., Maitra C., Paul B., Paul B. C., 2013, *MNRAS*, 436, 945
- Pradhan P., Maitra C., Paul B., Islam N., Paul B. C., 2014, *MNRAS*, 442, 2691
- Pradhan P., Paul B., Paul B. C., Bozzo E., Belloni T. M., 2015, *MNRAS*, 454, 4467
- Pradhan P., Bozzo E., Paul B., 2018, *A&A*, 610, A50
- Pradhan P., Bozzo E., Paul B., Manousakis A., Ferrigno C., 2019, *ApJ*, 883, 116
- Pradhan P., Raman G., Paul B., 2019, *MNRAS*, 483, 5687
- Pradhan P., Maitra C., Paul B., 2020, *ApJ*, 895, 10
- Rahoui F., Chaty S., Lagage P.-O., Pantin E., 2008, *A&A*, 484, 801
- Reig P., 2011, *Ap&SS*, 332, 1
- Reig P., Nespoli E., 2013, *A&A*, 551, A1
- Reig P., Chakrabarty D., Coe M. J., Fabregat J., Negueruela I., Prince T. A., Roche P., Steele I. A., 1996, *A&A*, 311, 879
- Reig P., Negueruela I., Papamastorakis G., Manousakis A., Kougentakis T., 2005, *A&A*, 440, 637
- Reynolds A. P., Bell S. A., Hilditch R. W., 1992, *MNRAS*, 256, 631
- Reynolds A. P., Quaintrell H., Still M. D., Roche P., Chakrabarty D., Levine S. E., 1997, *MNRAS*, 288, 43
- Riquelme M. S., Torrejón J. M., Negueruela I., 2012, *A&A*, 539, A114
- Rivers E. et al., 2010, *ApJ*, 709, 179
- Rothschild R. E. et al., 2017, *MNRAS*, 466, 2752
- Sadakane K., Hirata R., Jugaku J., Kondo Y., Matsuoka M., Tanaka Y., Hammerschlag-Hensberge G., 1985, *ApJ*, 288, 284
- Sasano M., Makishima K., Sakurai S., Zhang Z., Enoto T., 2014, *PASJ*, 66, 35
- Sguera V. et al., 2006, *ApJ*, 646, 452
- Sidoli L., Paizis A., 2019, in Oskinova L. M., Bozzo E., Bulik T., Gies D. R., eds, *Proc. IAU Symp. 346, High-mass X-ray Binaries: Illuminating the Passage from Massive Binaries to Merging Compact Objects*. Cambridge University Press, Cambridge . p. 178
- Sidoli L., Esposito P., Ducci L., 2010, *MNRAS*, 409, 611
- Sidoli L. et al., 2013, *MNRAS*, 429, 2763
- Staubert R., 2003, *Chin. J. Astron. Astrophys.*, 3, 270
- Staubert R., Klochov D., Wilms J., Postnov K., Shakura N. I., Rothschild R. E., Fürst F., Harrison F. A., 2014, *A&A*, 572, A119

- Staubert R. et al., 2019, *A&A*, 622, A61
- Staubert R., Ducci L., Ji L., Fürst F., Wilms J., Rothschild R. E., Pottschmidt K., Brumback M., Harrison F., 2020, *Astronomy & Astrophysics*, A196, 0004
- Steele I. A., Negueruela I., Coe M. J., Roche P., 1998, *MNRAS*, 297, L5
- Suchy S. et al., 2011, *ApJ*, 733, 15
- Suchy S., Fürst F., Pottschmidt K., Caballero I., Kreykenbohm I., Wilms J., Markowitz A., Rothschild R. E., 2012, *ApJ*, 745, 124
- Takahashi T. et al., 2007, *PASJ*, 59, 35
- Tanaka Y., 1986, in Mihalas D., Winkler K.-H. A., eds, *Lecture Notes in Physics*, Vol. 255, IAU Colloq. 89: Radiation Hydrodynamics in Stars and Compact Objects. Springer-Verlag, Berlin, p. 198
- Thompson T. W. J., Rothschild R. E., 2009, *ApJ*, 691, 1744
- Tomsick J. A., Chaty S., Rodriguez J., Foschini L., Walter R., Kaaret P., 2006, *ApJ*, 647, 1309
- Torrejón J. M., Schulz N. S., Nowak M. A., Kallman T. R., 2010, *ApJ*, 715, 947
- Trümper J., Pietsch W., Reppin C., Sacco B., 1977, *Annals of the New York Academy of Sciences*, 538, 0077
- Tsygankov S. S., Lutovinov A. A., 2005, *Astron. Lett.*, 31, 88
- Vasylenko A. A., Zhdanov V. I., Fedorova E. V., 2015, *Ap&SS*, 360, 37
- Walter R., Lutovinov A. A., Bozzo E., Tsygankov S. S., 2015, *A&AR*, 23, 2
- White N. E., Swank J. H., Holt S. S., 1983, *ApJ*, 270, 711
- Wijnands R., Degenaar N., Armas Padilla M., Altamirano D., Cavecchi Y., Linares M., Bahramian A., Heinke C. O., 2015, *MNRAS*, 454, 1371
- Wilson C. A., Finger M. H., Coe M. J., Laycock S., Fabregat J., 2002, *ApJ*, 570, 287
- Wilson C. A., Finger M. H., Coe M. J., Negueruela I., 2003, *ApJ*, 584, 996
- Wu Q., Gu M., 2008, *ApJ*, 682, 212
- Yoshida Y., Kitamoto S., Suzuki H., Hoshino A., Naik S., Jaisawal G. K., 2017, *ApJ*, 838, 30

**APPENDIX A:**

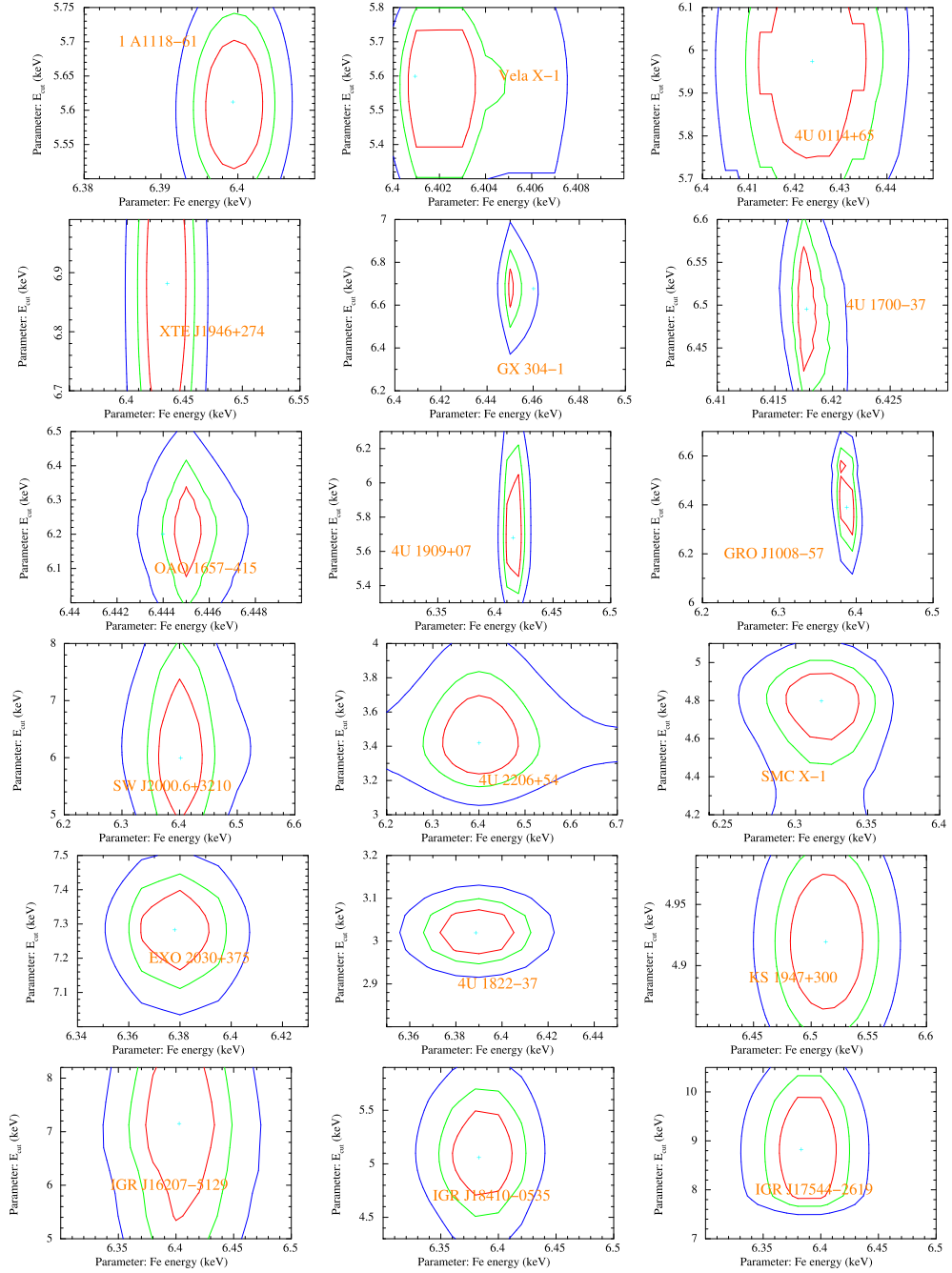


**Figure A1.** Contour plots between cut-off energy and iron line energy for sources in group 2 where these two values are close to each other. Note that for most of the sources, the iron line energy is centred at the neutral  $K\alpha$  line energy of 6.4 keV.

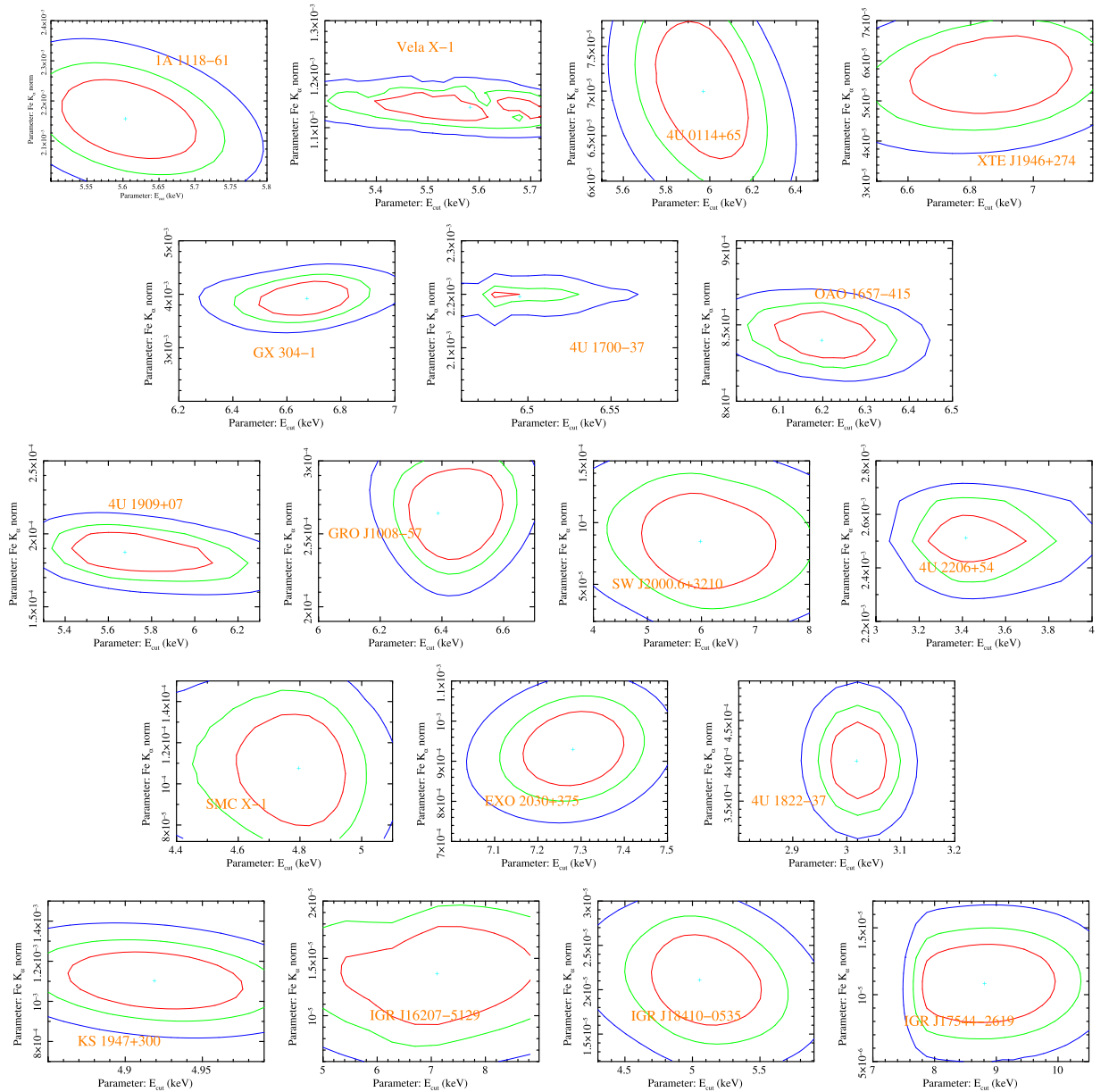


**Figure A2.** Contour plots between cut-off energy and iron line normalization for sources in group 2 (magenta) where these two values are close to each other.

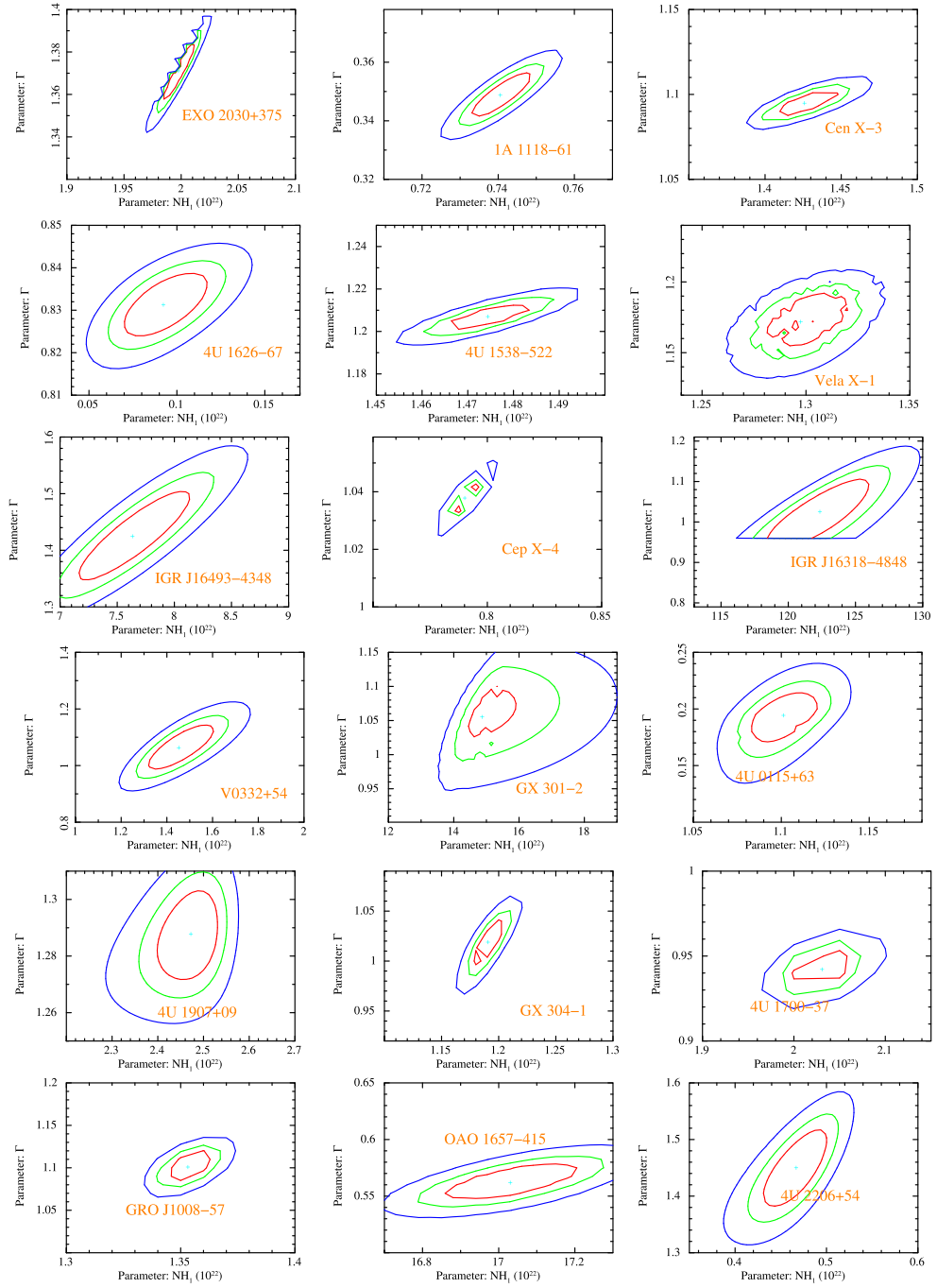


**Figure A3.** Contour plots between  $N_{\text{H1}}$  and gamma.



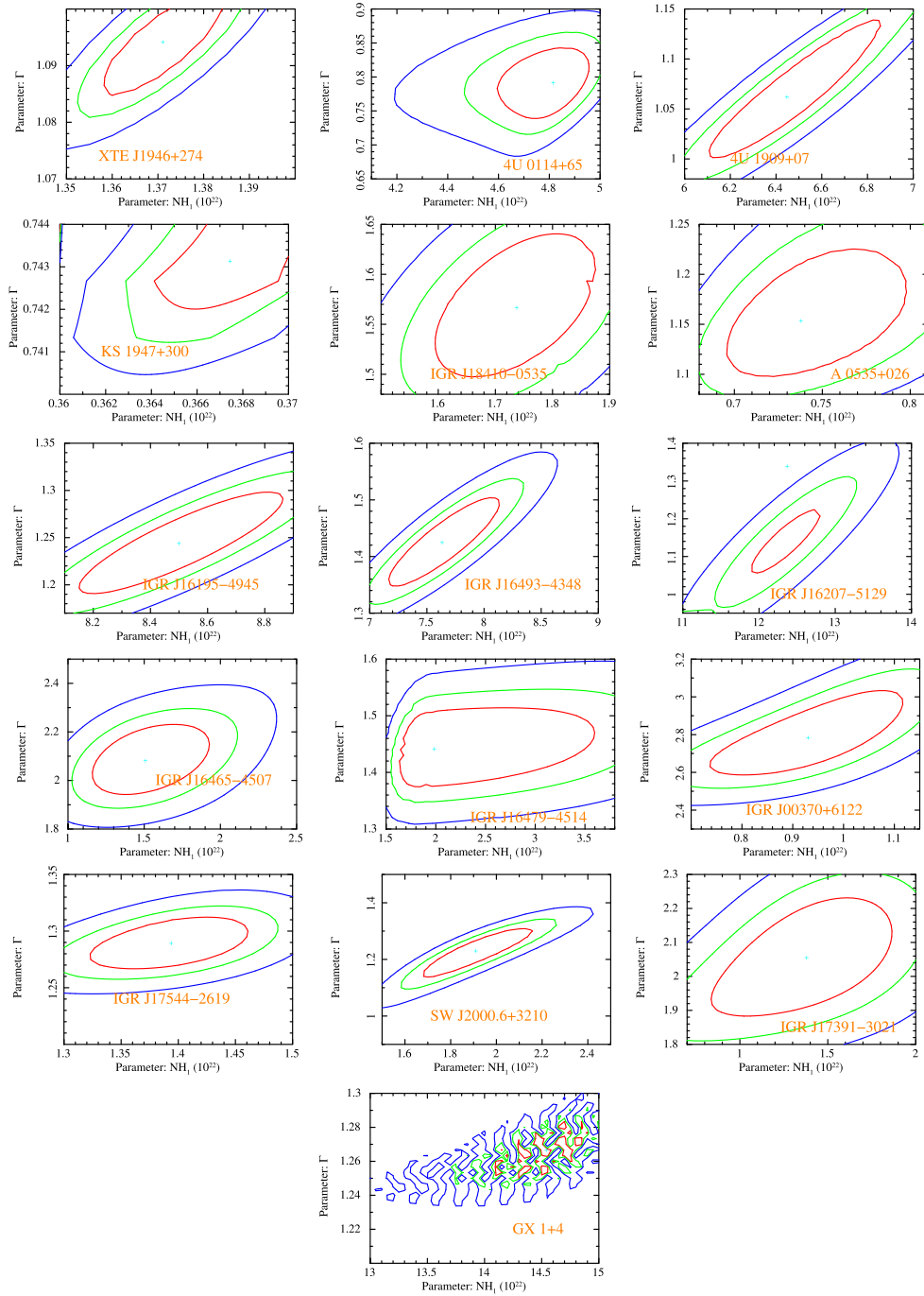
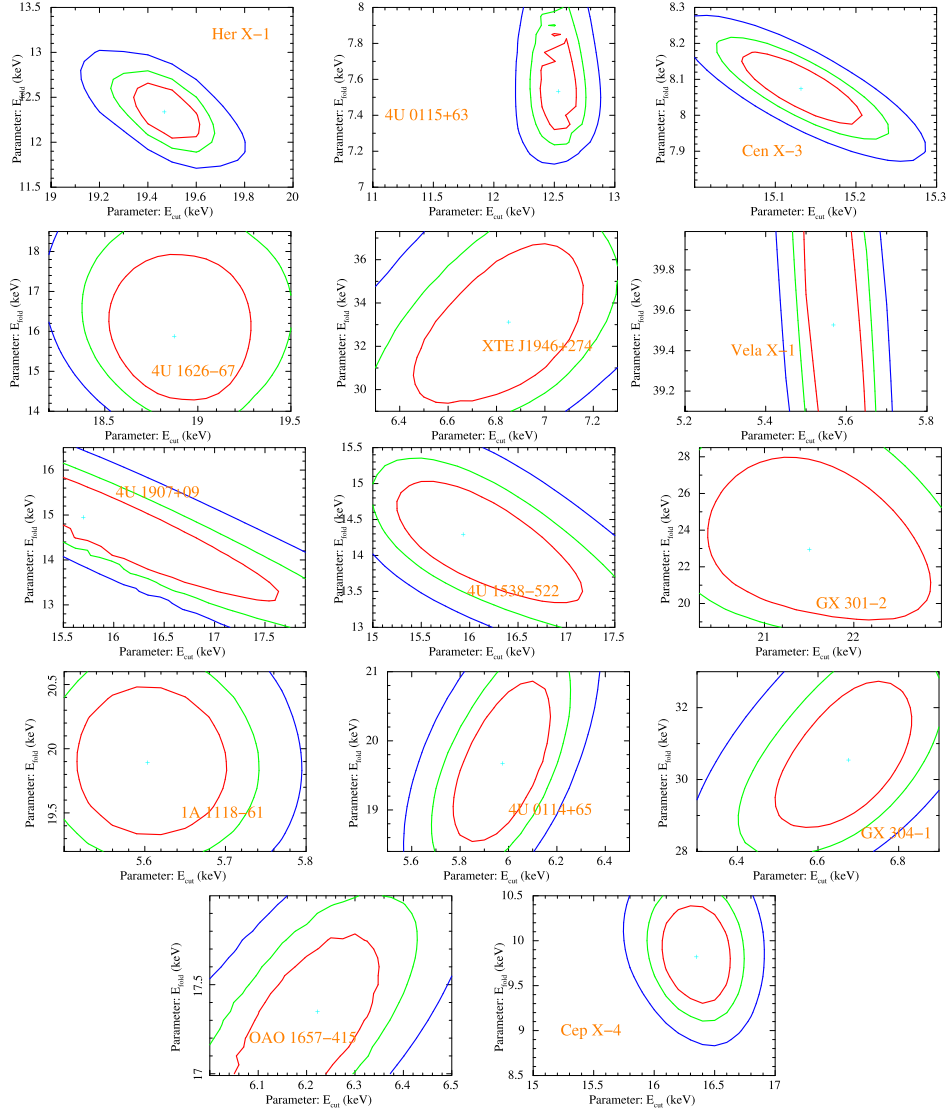


Figure A4. Contour plots between  $NH_1$  and  $\gamma$ .



**Figure A5.** Contour plots between cut-off energy and folding energy.

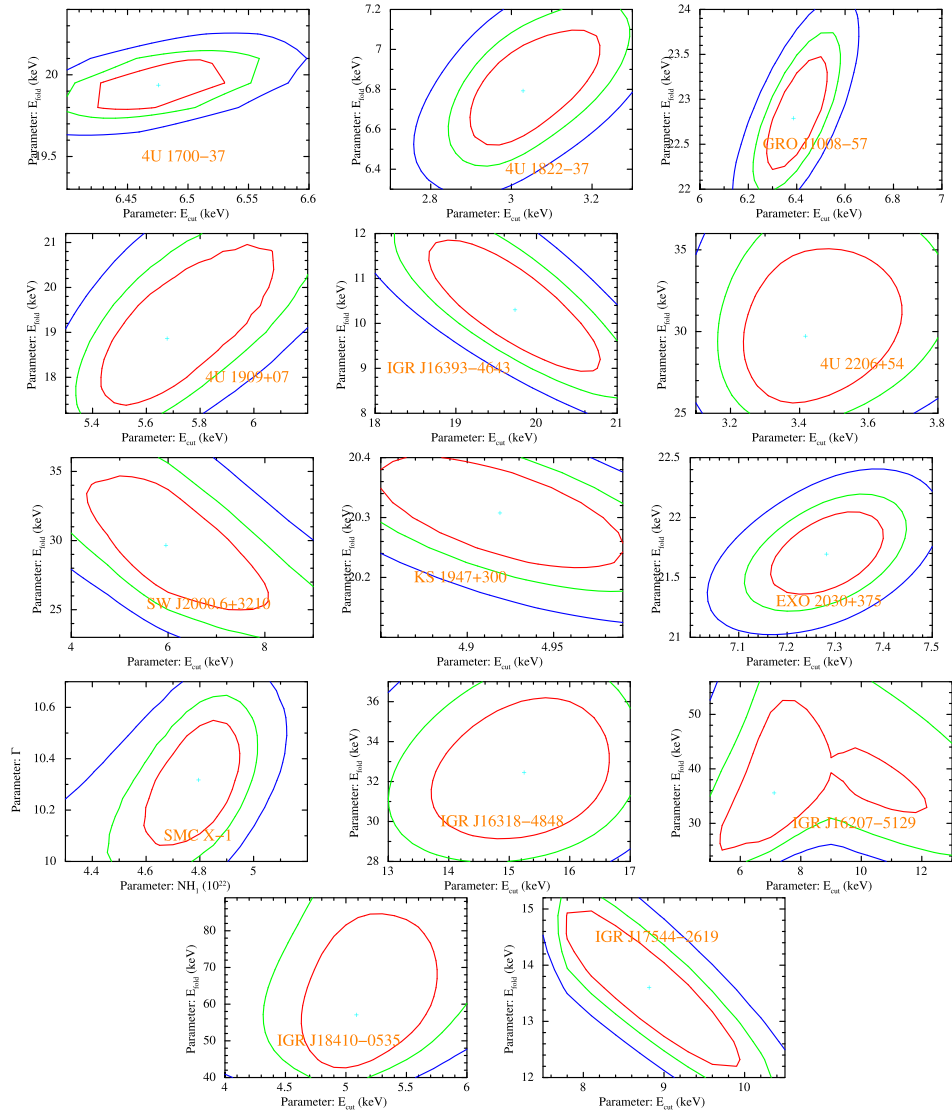
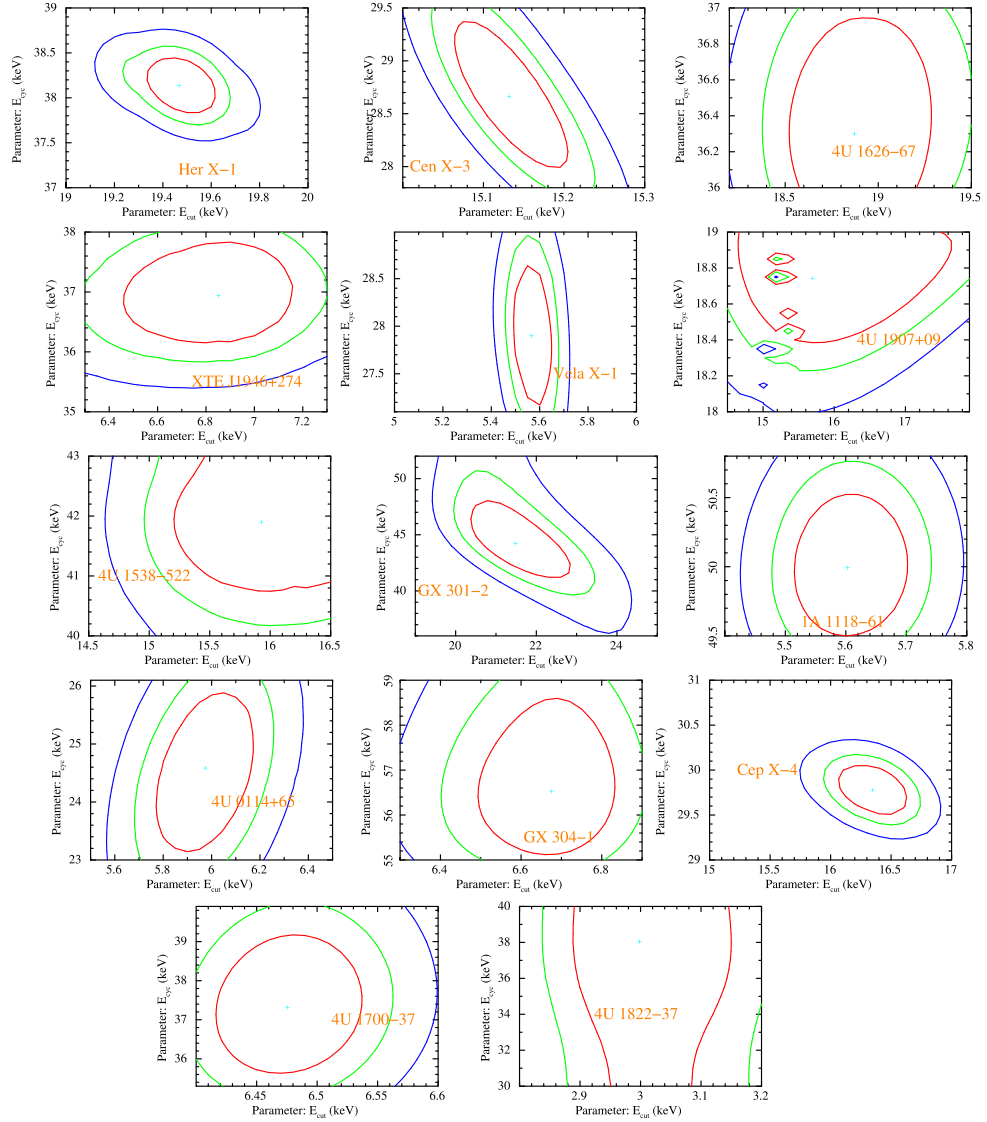


Figure A6. Contour plots between cut-off energy and folding energy.



**Figure A7.** Contour plots between cut-off energy and cyclotron line energy.

This paper has been typeset from a  $\text{\TeX}/\text{\LaTeX}$  file prepared by the author.